



HAL
open science

Physically-constrained data-driven inversions to infer the bed topography beneath glaciers flows. Application to East Antarctica

Jerome Monnier, Jiamin Zhu

► To cite this version:

Jerome Monnier, Jiamin Zhu. Physically-constrained data-driven inversions to infer the bed topography beneath glaciers flows. Application to East Antarctica. 2021. hal-01926620v3

HAL Id: hal-01926620

<https://hal.science/hal-01926620v3>

Preprint submitted on 19 Feb 2021 (v3), last revised 7 Jun 2021 (v4)

HAL is a multi-disciplinary open access archive for the deposit and dissemination of scientific research documents, whether they are published or not. The documents may come from teaching and research institutions in France or abroad, or from public or private research centers.

L'archive ouverte pluridisciplinaire **HAL**, est destinée au dépôt et à la diffusion de documents scientifiques de niveau recherche, publiés ou non, émanant des établissements d'enseignement et de recherche français ou étrangers, des laboratoires publics ou privés.

Physically-constrained data-driven inversions to infer the bed topography beneath glaciers flows. Application to East Antarctica

Jérôme Monnier · Jiamin Zhu

Received: date / Accepted: date

Abstract A method to infer the bed topography beneath glaciers from surface measurements (elevation from altimetry and velocity from InSAR) plus sparse thickness measurements is developed and assessed. The method relies on an original non-isothermal Reduced Uncertainty (RU) version of the Shallow Ice Approximation (SIA) equation which natively integrates the surface measurements. The flow model presents a single dimensionless multi-physics parameter γ ; it takes into account basal slipperiness and varying vertical rate factor profiles (therefore the vertical thermal variations). Next, the inversions rely on three stages involving: an Artificial Neural Network (ANN) and two Variational Data Assimilation (VDA) processes. The ANN based stage aims at estimating the multi-physics number γ from the thickness measurements; the resulting estimator is remarkably robust. The complete inversion method is valid for moderately sheared flows (presenting a moderate basal slipperiness): it can be applied to inland ice-sheets areas. Numerical results are presented in East Antarctica Ice Sheet areas where the bed elevation may be highly uncertain (Bedmap2 values). The estimations are valid for wave lengths greater than $\sim 10\bar{h}$ (due to the long wave assumption, shallow flow model) with a resolution at $\sim \bar{h}$ (\bar{h} a characteristic thickness value).

Keywords Variational data assimilation · reduced flow model · deep learning · inference · topography · glaciers · Antarctica.

1 Introduction

Bed topography elevation is a necessary data to set up dynamic ice flow models. Also, when combined with the surface topography measurements (e.g. acquired by altimetry), it straightforwardly provides the ice volume. In Antarctica and Greenland ice-sheets, ice thickness measurements are available along airborne radio-echo sounding tracks e.g. in the CReSIS RDS database¹. These measurements are particularly dense in fast ice coastal stream areas. On the contrary, they are very sparse inland; they are even nonexistent deep inland, see [4, 14] and references therein.

Numerous satellites provide (or have provided) accurate measurements of ice sheets surfaces: altimeters provide surface elevation H at $\approx \pm 20$ cm for 1 km² pixels see e.g. [22, 4], radar interferometers (InSar) provide surface velocity \mathbf{u}_H see e.g. [43].

To obtain the bed elevation values beneath the glaciers, the challenge is next to infer its value between the thickness measurements given the surface measurements.

A simple method to try to solve this challenge is to apply an ordinary Kriging, a statistical interpolation method (the most employed in geo-statistics). This interpolation method (purely data-driven) may be viewed as a Gaussian process regression providing the best linear unbiased prediction. This method is the one employed to provide the reference bed elevation estimations in large vicinities of measurements in Greenland and Antarctica, see [3, 14]. For estimations in Antarctica, the authors of [14] suggest that for cells located less than 20km from a measurement, the estimation error is an increasing function of the distance at a given rate. Next, beyond 20 km, the error would be uncorrelated with the distance. Still in the reference map called Bedmap2 [14], for cells located more than 50 km from any measurement, the thickness estimation is based on the gravity-field inversion. As a consequence, the estimations far from any measurements present very large uncertainties, up to $\pm \sim 1000$ m according to [14].

J. Monnier
INSA & Institut de Mathématiques de Toulouse (IMT), France
E-mail: jerome.monnier@insa-toulouse.fr

J. Zhu
INSA & Institut de Mathématiques de Toulouse (IMT), France

¹ CReSIS RDS Data <http://data.cresis.ku.edu> (NASA, NSF, Kansas fundings).

To reduce uncertainties on the bed elevation beneath ice-sheets, combining physically-informed models and datasets is definitively a good direction. To do so, a key-point is to employ a flow model sufficiently complex to be representative enough but simple enough to lead to well-posed, stable inverse problems (i.e. not leading to severe equifinality issues). In inverse geophysical flows modeling, equifinality issues are the common pitfall to avoid, see e.g. [5].

In fast ice streams ($\approx 1 - 10$ km/y in Antarctica), the flows are plug-like (the glaciers simply slide). In this case, the momentum equation becomes trivial and inverting the (depth-integrated) mass equation enables to fill up the gaps downstream (and upstream) the measurements, see [46,40]. Due to the depth-integrated mass equation nature, the measurements (e.g. the flight tracks during airborne campaigns) have to be acquired cross-lines and relatively densely. Indeed, it is well known that this transport equation is intrinsically unstable when inverted; moreover, it propagates errors, see e.g. [36] and references therein. To locally damp this feature, some artificial diffusion which regularizes the equation has to be introduced. The inversion of the mass equation has been proposed in [8,46]; next, it has been combined with surface measurements by Variational Data Assimilation (VDA) in [41,42]. This approach has enabled the estimation of the bed elevation under ice streams, in particular in Greenland [40,42].

In [7], a Bayesian framework is applied to provide probability distributions of thickness assuming Gaussian covariance structures of input data. The algorithm is equivalent to ordinary Kriging if no prior data is available. Bayesian approaches are particularly rich, however again here it relies here on mass conservation only.

For fully sheared flows, the isothermal Shallow Ice Approximation (SIA) flow model with no slip at bottom, has been inverted in [37,21]. These estimations are robust however they are relevant for a very restricted flow regime only: fully sheared flow areas (therefore very slow flows, $\approx 1 - 10$ m/y in Antarctica).

In moderately sliding flows, equivalently moderately sheared flows (that is mid-sliding mid-sheared), the slipperiness at bottom has to be taken into account in the inversion; it is an additional unknown parameter, in addition to the rate factor modeling the internal deformation. Inversions in such flow regime are much more challenging than the ones in the two previously described regimes. The inverse problem is here a-priori ill-posed.

Let us cite some other studies related to bedrock estimations. [25] inverts the 1D depth-integrated SIA equation with slipperiness and a shape factor which models the 3D features of the flow. This leads to an ill-posed inverse problem; however, the inversions are performed by imposing empirical constant values for the few unknown parameters. Based on the inversion of the complete hybrid SIA-SSA system called PISM [55] (SSA for Shallow Shelf Approximation), [51] uses an empirical iterative method to calibrate the bed elevation only. In [38], the SIA flow model with slipperiness at bottom (i.e. not no-slip) is inverted by distinguishing different sub-regimes. The developed mid-analytical mid-computational inversion methods lead to well-posed inverse problems, therefore stable inversions. The only weakness of the study arises in the ice rate factor which is supposed to be constant. Unfortunately this assumption is unrealistic for ice-sheets.

Inland ice-sheets areas presenting mid-range surface velocities ($\approx [10 - 100]$ m/y in Antarctica) correspond to moderately slipping / moderately sheared flows. Such flows cannot be accurately modeled neither by mass conservation only, nor by plug-like flows models (e.g. SSA model), nor by fully sheared flows models (e.g. the classical SIA model with no slip at bottom). In this case, the measured surface features (elevation and velocity) are the signature of the slipperiness at bottom *and* the internal deformation. Moreover, the internal deformation depends on the constitutive ice behavior *and* the vertical thermal profiles. As a consequence, to invert the surface data in moderately sheared flows is highly challenging. Moreover, inland moderately sheared flows have been poorly covered during the airborne campaigns since they constitute large and far areas therefore difficult and expensive to flight over. As a consequence, the flow model to invert needs to be stable and robust when inverted even in lack of local in-situ data. This mathematical property is all but trivial to obtain, see e.g. [2,36,48,38]. Moreover, it would be highly valuable that the flow model inversion is as insensitive as possible to the measurements locations.

Note that an *effective* bed topography only can be inferred from the surface signature. Indeed, the glaciers flows act as low-band filters: the bed variations are filtered by the flow with filtering features depending on the flow regime, see [18,34,35] for detailed analysis. Given a flow regime and a flow model, this corresponds to an inferable minimal wave length [19,34,35].

Finally, let us mention that a comparison of various inverse methods to estimate the bed elevation beneath glaciers (equivalently the ice thickness) is presented in [12]. The comparison relies on numerous test cases representing a large spectrum of ice flow regimes. For all test cases, no prior thickness value is supposed to be known. The 15 inter-compared methods are classified by resolution type and not by domain of validity of the method (e.g. in function of the flow regime). Numerical comparisons are presented; however, no analysis of the equifinality issues is proposed.

The present study aims at solving the following inverse problem: estimating the ice thickness (equivalently the bed elevation) in mid-sheared mid-sliding flows with a hybrid physically-informed data-driven method. The targeted flow regimes requires to take into account the complete physics of the flows. To do so, a key ingredient is the RU-SIA (RU for Reduced Uncertainties) model derived in [39]. This flow model is dedicated to the present inverse problem by intrinsically ("natively") integrating the surface measurements in its coefficients. It is a complete multi-physics flow model, depth-integrated (shallow flow, long-wave assumption); it respects a "well-balanced complexity" in view to invert it. It

99 takes into account both mass and momentum conservations, with a temperature dependent rate factor: the internal deformation is non-uniform, it depends in particular to the vertical temperature profiles. In the RU-SIA model, all the complex
100 multi-physics phenomena are consistently represented by a new *dimensionless parameter* (denoted by γ).

101 The inversion method developed here is based on a combination of VDA algorithms and a purely data-driven inversion,
102 actually like in our previous study [39]. However in the single test case analyzed in [39], a clear correlation was existing
103 between γ and one of the observable field (namely $|\mathbf{u}_H|$), see [39] Fig. 7. In these conditions, estimating γ by a simple
104 Kriging method was possible. Next, when applying the method to other areas (e.g. those considered in the present study),
105 it turned out that such correlations were not existing. Therefore an other method to attempt to estimate this dimensionless
106 multi-physics parameter γ had to be investigated. This is successfully done here by using a Neural Network Residual
107 Kriging (NNRK) algorithm, see [11,30]. As a consequence, a new inversion method to infer the bed elevation is here
108 presented. The employed data are still the surface measurements (elevation, velocity) plus some local in-situ thickness
109 values. The inversion method relies on the RU-SIA equation derived in [39], a first advanced VDA process, a deep
110 Artificial Neural Network (ANN) and a last VDA process which enables to conclude. The ANN aims at estimating the
111 dimensionless multi-physics parameter γ of the RU-SIA model from the in-situ ice thickness measurements. These in-situ
112 measurements are available along flight tracks of airborne campaigns. The complete inversion method is demonstrated
113 to be mathematically and computationally robust. The considered areas are the EAIS regions which a-priori respect the
114 domain of validity of the flow model; this corresponds to six large inland East Antarctica Ice Sheet (EAIS) regions. In
115 other respects, let us recall that estimating accurately the bed elevation in EAIS is interesting since global warming may
116 threaten its stability, particularly around some of the considered areas, see [13].

117 Moreover a remarkable relationship between the present inversions based on the RU-SIA flow model and the mass conservation
118 method, largely developed in [46,40,42], is presented. This relationship opens promising perspectives to complete
119 the mass conservation based estimations only, in deeper ice-sheets regions. Indeed, we mathematically show that the
120 present complete estimations and the mass conservation only estimations are connect each other at the interface of their
121 respective domain of validity, that is at the plug-like flows boundaries (e.g. at sheared margins and further).

122 The present inversion method may be applied to any glaciers flows as soon as the flow model assumption is satisfied (that
123 is from highly sheared flows to mid-sheared mid-sliding ones). Due to the long wave assumption of the flow model, the
124 thickness estimations are valid at $\approx 10 \times \bar{h}$ wave length, \bar{h} a characteristic thickness value.
125

126
127 The outline of the article is as follows. In Section 2, the RU equation developed in [38,39] is recalled; its domain
128 of validity is highlighted; uncertainty of the dimensionless parameter γ is analyzed. Next, the inversion method is de-
129 tailed: Step 1) and Step 3) of the global algorithm aim at inverting the RU-SIA equation by VDA (physicalled-informed
130 inversions); Step 2) aims at estimating γ using a NNRK algorithm (deep learning, purely data-driven). In Section 4, the
131 considered six large EAIS areas (named Ant p , $p = 1, \dots, 6$) are presented. The methods to obtain the reference Bedmap2
132 estimations [14] are briefly recalled. Each computational steps of the present inversion method is analyzed in detail.
133 In Section 5, the robustness of the estimations is assessed in details for the Ant1 and Ant3 cases, in particular their
134 sensitivities with respect to the presence or not of additional flight tracks. A conclusion is proposed in Section 6. As
135 complimentary material, the computed thickness estimations for four other areas Ant p , $p = 2, 4, \dots, 6$, are presented in
136 Appendix.

137 2 Method

138 In this section the inversion method to estimate the ice thickness h (equivalently the bed topography elevation b) is de-
139 tailed. It is done in three steps. Step 1) aims at estimating the product (γh) by assimilating all surface data (altimetry,
140 InSAR and climatic term Source Mass Balance) plus the in-situ thickness measurements in the RU-SIA flow model
141 (model presented below). Step 2) aims at estimating the dimensionless multi-physics parameter γ from the in-situ mea-
142 surements only (measurements available along the flight tracks of airborne campaigns). Step 3) aims at estimating the
143 thickness h (and adjusting a climatic term) by assimilating all available data again. The final output of the inversion
144 method is the ice thickness h , therefore the bed topography elevation b .
145

146 2.1 The RU-SIA flow model

147 The RU-SIA equation is obtained by reformulating the depth-integrated SIA model with basal slipperiness (see e.g. [17]
148 Chapter 5) but with a non constant rate factor and by natively integrating the surface measurements (elevation and veloc-
149 ity). The resulting 2D depth-integrated flow model is original; it is relevant for large scale sheared flows with moderate
150 slipperiness at bottom and with non constant vertical temperature profile. The various uncertain multi-physics param-
151 eters (constitutive law exponent, flow regime, temperature dependent term) are gathered into the single dimensionless

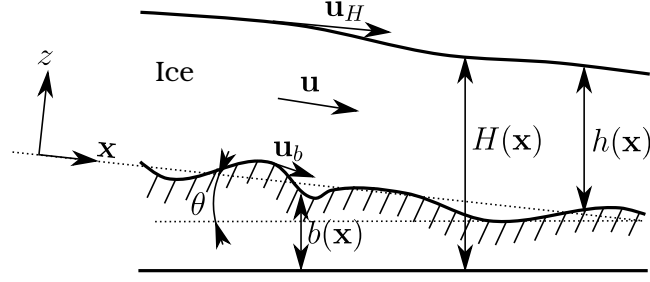


Fig. 1 Schematic vertical view of the gravitational ice flow and notations

152 parameter γ . As a consequence, all the physical parametrisation uncertainty is represented by this original dimensionless
 153 parameter. The basic RU-SIA model assumptions are the same as those for the SIA model (classical lubrication the-
 154 ory) with basal slipperiness that is: the flow is necessarily sheared (normal stress components are negligible) and it is
 155 "shallow" (long wave assumption).

156 2.1.1 The equations and the dimensionless parameter γ

157 The surface slope is denoted by $\mathcal{S} = |\nabla H|$; \mathbf{u}_H is the surface velocity and \mathbf{u}_b is the velocity at bottom (basal velocity).
 158 The depth (ice thickness) is denoted by h , $h = (H - b)$ with H the ice surface elevation and b the bed elevation, see Fig.
 159 1. θ is a potential mean slope value in the (x, y) -plane ($\theta = 0$ in the forthcoming test areas).
 160

161 *The flow equation.* The depth-integrated flow model SIA model with slipperiness at bottom (see e.g. [17] Chapter 5) is
 162 derived in a non isothermal case in [38] providing the so-called xSIA (x for extended) equation. Next in [39], by taking
 163 advantage of the measured surface features (elevation and velocity norm), the xSIA model is re-formulated to obtain the
 164 RU-SIA model. The RU-SIA equation reads as follows:

$$-div \left(\frac{|\mathbf{u}_H|}{\mathcal{S}} \gamma h \nabla H \right) (\mathbf{x}) = \dot{a}(\mathbf{x}) \text{ in } \Omega \quad (1)$$

165 \mathbf{x} denotes the space variable and Ω the considered domain (an open set of \mathbb{R}^2). The RHS \dot{a} is the classical one defined
 166 by: $\dot{a}(\mathbf{x}) = (\partial_t h - a)(\mathbf{x})$ with a the mass balance (accumulation and ablation), see e.g. [17].
 167

168 In (1), the term $\frac{|\mathbf{u}_H|}{\mathcal{S}}$ is the observational term; it may provided by InSAR and altimetry surface measurements.
 169 The considered unknown of (1) is the surface elevation H . (1) is a linear diffusive equation in H , it is closed by Dirichlet
 170 condition at boundaries: H given e.g. by altimetry.
 171 Assuming that h (or equivalently b) is given, (1) contains γ as the single uncertain parameter.
 172

173 *The dimensionless parameter:* γ is the dimensionless parameter of the equation, its expression is, [39]:

$$\gamma(\mathbf{x}) = \left(1 - \frac{c_A(\mathbf{x}) R_s(\mathbf{x})}{(q+2)} \right) \quad (2)$$

174 R_s is the slip ratio describing the flow regime; it is defined as: $R_s(\mathbf{x}) = 1 - \frac{|\mathbf{u}_b|}{|\mathbf{u}_H|}(\mathbf{x})$.

175 The parameter c_A is defined by:

$$c_A(\mathbf{x}) = [(q+2) - (q+1)R_A(\mathbf{x})] \quad (3)$$

176 where q is the constitutive power-law exponent ($q = 3$ in the classical Glen's law, see e.g. [17] Chapter 5, [38]) and
 177 $R_A(\mathbf{x}) = \frac{\bar{A}(\mathbf{x})}{\underline{A}(\mathbf{x})}$.

178 The parameters $\bar{A}(\mathbf{x})$ and $\underline{A}(\mathbf{x})$ are the depth-integrated quantities naturally appearing if the rate factor A depends on
 179 (\mathbf{x}, z) . Their expressions are as follows, see [38]:

$$\bar{A}(\mathbf{x}) = \frac{(q+2)}{h^{q+2}(\mathbf{x})} \left(\int_b^H \int_b^z A(\mathbf{x}, \xi) (H(\mathbf{x}) - \xi)^q d\xi dz \right)^{-1} \quad (4)$$

180

$$\underline{A}(\mathbf{x}) = \frac{(q+1)}{h^{q+1}(\mathbf{x})} \int_b^H A(\mathbf{x}, z) (H(\mathbf{x}) - z)^q dz \quad (5)$$

181

If the vertical profile of A is constant (A constant in z) then: $\bar{A}(\mathbf{x}) = A(\mathbf{x}) = \underline{A}(\mathbf{x}) \forall \mathbf{x}$.

182

Recall that the rate factor A models internal structure properties of the ice. A depends on ice temperature, crystal orientation, debris content, etc. It may be represented by the Arrhenius law, see e.g. [17] Chapter 4 and references therein. This parameter A highly depends on the temperature, [17], therefore in particular on z in ice sheets.

186

Isothermal case. In the isothermal case, A is classically supposed to be a constant, see e.g. [17] Chapter 5. As a consequence, in this case we obtain: $\bar{A}(\mathbf{x}) = A = \underline{A}(\mathbf{x}) \forall \mathbf{x}$. It follows that: $R_A(\mathbf{x}) = 1 = c_A(\mathbf{x}) \forall \mathbf{x}$.

188

189

Next for the classically employed value $q = 3$, it follows: $\gamma(\mathbf{x}) = (1 - \frac{1}{5}R_s(\mathbf{x}))$.

190

191 2.1.2 Domain of validity of the model

The shallowness of the flow is estimated through the geometrical ratio $\varepsilon = \frac{H^*}{L^*}$, where H^* and L^* are characteristic flow depth and length respectively. In these depth-integrated asymptotic models, ε has to be small enough, $\varepsilon \lesssim 1/10$ at least, see e.g. [29]. As a consequence this flow model is valid for a minimal wave length $L^* \gtrsim 10H^*$. The flow regime is characterised by the slip ratio R_s . By construction, the SIA-like models (including xSIA and RU-SIA equations) are valid for R_s ranging from ≈ 0.3 to 1, see [23,47,6] for detailed analysis. This estimation in terms of R_s is numerically quantified in real world cases (including EAIS) in [54]. This study is based on the so-called MCL criteria (criteria proposed in [24] and defined as the length scale over which the terms of driving stress and drag are comparable). In particular it can be noticed that the ice-sheet areas presenting surface velocity ranging in $\approx [5 - 100]$ m/y are accurately modelled by the SIA model as soon as the minimal wave length equals $\approx 10 - 12$ km in mean. The six test areas Antp considered in the next sections, see Fig. 4, have been defined from the surface velocities norm values: $|\mathbf{u}_H| \in \approx [10 - 80]$ m/y. In these cases $H^* \approx 2 - 3$ km, then the RU-SIA equation is accurate for minimal wave lengths $L^* \approx 20 - 30$ km.

203

204 2.1.3 Relationship with the mass equation & its inversion in fast plug-like flows

As already mentioned, nice bed elevation estimations are obtained in fast streams by simply inverting the depth-averaged mass equation $div(h\bar{\mathbf{u}}) = \dot{a}$, $\bar{\mathbf{u}}$ the depth-averaged velocity, see [42]. In [46,41,42], $\bar{\mathbf{u}}$ is related to \mathbf{u}_H as $\bar{\mathbf{u}} = \tilde{\alpha}\mathbf{u}_H$, with $\tilde{\alpha}$ set empirically. In fast streams (actually plug like flows), we have $R_s \sim 0$ and $\tilde{\alpha} \lesssim 1$. Therefore, for such cases the uncertainty on the internal deformation (represented in the RU-SIA equation by the parameter c_A) is negligible. As a consequence $\tilde{\alpha}$ may be set close to 1 with a few percent error only. This is what is done in these aforementioned studies. In other respect, we can show that: $\bar{\mathbf{u}} = -\frac{|\mathbf{u}_H|}{\mathcal{S}}\gamma\nabla H$, see [39]. Therefore if the slopes $\mathcal{S} = |\nabla H|$ and the velocity are co-linear (this is a commonly admitted assumption) than the parameter $\tilde{\alpha}$ empirically defined in [46,41] is nothing else than the dimensionless parameter γ defined by (2).

210

211

212

213

214

215

216

217

218

This equality $\gamma = \tilde{\alpha}$ enables building up continuous estimations between fast plug-flows (obtained by inverting the mass equation like in [41,42]) and the moderately sheared / moderately sliding flows (obtained by inverting the present RU-SIA equation).

On the contrary to plug like flows, in moderately sheared / moderately sliding flows, γ varies importantly therefore setting its value empirically is not reasonable anymore. That is why an actual estimation of γ is required.

219 2.2 On the uncertainty range of parameter γ

The dimensionless parameter γ defined by (2) depends on various physics parameters: the constitutive law exponent q , the vertical temperature profile through the rate factor $A(z)$ and the flow regime (slip ratio R_s). Recall that the RU-SIA model domain of validity corresponds to $R_s \in [\approx 1./3., 1]$, see [23,47,6]. For sake of simplicity, q is supposed to be set to the widely employed value for glaciers flows, that is $q = 3$ (Glen's law). In isothermal cases, it follows that: $\gamma(\mathbf{x}) = (1 - 0.2R_s(\mathbf{x}))$. Therefore in isothermal cases, the uncertainty on γ is relatively small, $\approx 10\%$ only.

The large majority of glaciers are not isothermal in particular those in ice-sheets. Following the Arrhenius law, see e.g.

225

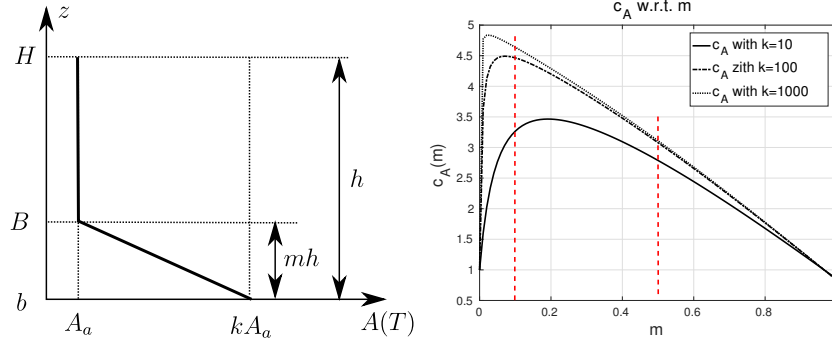


Fig. 2 (Left) A typical vertical profile of rate factor $A(\cdot, z)$, see (6). (Right) The parameter c_A vs m , see (3), with $k = 10, 100$ and 1000 .

226 [17, p.54], and by considering typical ice-sheet vertical temperature profiles in ice-sheets, see [44,45] and e.g. [27,49],
 227 we consider the following vertical profile of $A(\mathbf{x}, z)$, Fig. 2 (Left):

$$A(\cdot, z) = \begin{cases} A_a & \text{for } z \in [B(\cdot), H(\cdot)] \\ \frac{A_a}{(B-b)(\cdot, z)} ((1-k)z + kB(\cdot) - b(\cdot)) & \text{for } z \in [b(\cdot), B(\cdot)] \end{cases} \quad (6)$$

228 with A_a and k given constants. We define: $B(\mathbf{x}) = (mh(\mathbf{x}) + b(\mathbf{x})) \forall \mathbf{x}$ with $m \in [0, 1]$. Then $A(\mathbf{x}, z)$ presents a boundary
 229 layer at bottom of thickness $(B - b)(\mathbf{x}) = mh(\mathbf{x})$, Fig. 2 (Left). The value of $c_A(\mathbf{x})$ vs m for different values of k is pre-
 230 sented in Fig. 2 (Right). The case $m = 0$ corresponds to the isothermal case: $c_A = 1$. For thin thermal boundary layers c_A
 231 increases with mh ; for thicker layers c_A decreases to a minimal value $c_A^{(min)} \lesssim 1$. (This minimal value is reached for the
 232 purely linear vertical profile: $m = 1$).

233
 234 Let us consider typical temperature values in EAIS: the bed is at $0C^\circ$ and the surface at $-40C^\circ$. These values
 235 correspond to $A_a \approx 10^{-26}$ therefore $k \approx 1000$, see Fig. 2 (Right). (The value $k \approx 10$ would correspond to typical inland
 236 Greenland cases, see [39]). Assuming a boundary layer corresponding to $m \in [0.1, 0.5]$, it follows: $c_A \in (3.11, 4.64)$ (Fig.
 237 2). Finally it follows from (2) that: $\gamma(\mathbf{x}) \approx [1 - (0.78 \pm 0.15)R_s(\mathbf{x})]$.

238 This rough uncertainty analysis based on typical values in the targeted areas shows that the uncertainty on γ comes
 239 similarly from the vertical thermal profile uncertainty (represented by the term $(c_A/(q+2))$) and the slip ratio R_s . In the
 240 targeted regimes and EAIS areas with the vertical profile (6), this corresponds to γ varying within the interval $]0, \approx 0.7]$.
 241 If relaxing the assumption on the vertical profile as defined in (6), one may estimate the upper bound of γ by setting
 242 $c_A = 1$ and $R_s = 0.5$ which gives: $\gamma \in]0, \approx 0.9]$. (Recall that in fast plug-like flows, γ is close to 1).
 243 In the forthcoming numerical results, the estimations of γ by the NNRK algorithm are within intervals $]0, \approx 0.9]$, see e.g.
 244 figs. 6 and 9(Up)(Right).

245 2.3 The inversion method

246 The inversion method to estimate the ice thickness h is developed in three steps. Step 1) and Step 3) are physical-based
 247 inversions: the RU-SIA equation (1) is inverted with respect to the product (γh) at Step 1), with respect to (h, \dot{a}) at Step
 248 3). Step 2) is based on an Artificial Neural Network (ANN) aiming at estimating γ ; it is a purely data-driven inversion.

249 2.3.1 Sketch of the complete inversion method

250 The estimations of thickness are performed in three steps as follows.

Step 1) Estimation of the effective diffusivity $\eta = (\gamma h)$ in RU-SIA equation (1) by VDA.

252 Given the surface measurements (observations) H^{obs} and $|\mathbf{u}_H^{obs}|$, the effective diffusivity $\eta = (\gamma h)$ in (1) is inferred by
 253 solving the following optimal control problem:

$$\min_{\mathbf{k}} g(\mathbf{k}) \quad \text{with } g(\mathbf{k}) = g_{obs}(\mathbf{k}) + \alpha g_{reg}(\mathbf{k}) \quad (7)$$

254 with $\mathbf{k} \equiv \eta = (\gamma h)$ and

$$g_{obs}(\cdot) = \frac{1}{2} \int_{\Omega} |H(\cdot)(\mathbf{x}) - H^{obs}(\mathbf{x})|^2 \chi_{tr}(\mathbf{x}) d\mathbf{x}, \quad (8)$$

255 χ_{tr} is the spatial restriction operator to the flight tracks, $g_{reg}(\cdot)$ a Tykhonov's regularization term, see e.g. [28]. In
 256 this step, it is defined as: $g_{reg}(\eta) = \frac{1}{2} \int_{\Omega} |\nabla \eta(\mathbf{x})|^2 d\mathbf{x}$. The weight coefficient α is classically set such that it provides

a reasonable balance between the physical misfit and the regularization (regularization should be greatly lower than the physical misfit term). The surface elevation $H(\eta)$ corresponds to the solution of the RU-SIA equation (1) (with Dirichlet boundary conditions) with η given. The gradient of the cost functional is computed by introducing the adjoint equation. The minimisation algorithm is a quasi-Newton method (the L-BFGS algorithm of the Python routine `scipy.optimize.minimize`). The iterative minimization process is performed until convergence. Numerous numerical experiments have demonstrated robust convergences. In particular the optimal solution does not significantly depend on the smoothing length scale of the surface data (done in the present $Ant - p$ test cases at ≈ 24 km, see next Section), nor on the first guess (set to h_b the Bedmap2 value in EAIS).

Past this computational VDA step providing the optimal value η^* , the value of γ along the flights tracks where depth measurements h_b are available are straightforwardly deduced: $\gamma_{tr}^* = \frac{\eta^*}{h_b} \chi_{tr}(\mathbf{x})$. These values are inputs of the next algorithm, Step 2).

These obtained values are representative at the flow model scale, that is at $10\bar{h} \approx 25$ km minimal wave length (with ≈ 2 km mesh cells), see the investigation presented in [39].

Step 2) Extension of γ in the whole domain by NNRK.

Given γ_{tr}^* along the flights tracks (result of Step 1)), a NNRK algorithm ([11, 30]) is applied to extend values of γ to the whole area. This statistical learning algorithm is done in two steps: 1) an ANN estimator (deep learning) is built up; 2) an ordinary Kriging of the residuals is added. Details are presented in the next paragraph.

Step 3) Estimation of the pair (h, \dot{a}) in RU-SIA equation (1) by VDA.

Given γ all over the domain (result of Step 2)), the thickness h is inferred simultaneously with the RHS \dot{a} in (1) by another VDA process. Let us recall them briefly.

Similarly to Step 1), the pair (h, \dot{a}) in (1) is inferred by solving the optimal control problem (7) with g_{obs} defined by (8) but minimizing with respect to $\mathbf{k} = (h, \dot{a})$ (and not w.r.t. $\eta = \gamma h$ like in Step 1)). In this VDA process, the regularization term reads:

$$g_{reg}(h, \dot{a}) = \frac{1}{2} \|(h - h_b)\|_{C_h^{-1}} + \frac{1}{2} \|\dot{a} - \dot{a}_b\|_{C_a^{-1}} \quad (9)$$

with C_h^{-1} and C_a^{-1} covariance operators defining metrics, (h_b, \dot{a}_b) prior background values (equal to the current classical estimations). The latter are classically defined as the second order auto-regressive correlation matrices with length scale respecting a balance between the regularisation and the preconditioning effects of the VDA algorithm, see [20, 39]. Next following [33, 20], a change of the control variable is made. The numerous numerical experiments have demonstrated that this choice of covariance operators combined with the change of variable improves greatly the robustness and the convergence speed of the VDA algorithm. In (7) the weight coefficient α is defined as a decreasing sequence following an iterative regularisation strategy, see [28] for an analysis. This iterative regularisation strategy improves the convergence speed of the VDA algorithm too.

Numerous assessments of the VDA steps are presented in [39], in particular the sensitivity of the inversions with respect to: i) the uncertainties on γ ; ii) the density of flights tracks (by removing some of them); iii) the smoothing length scale of the surface data (altimetry, InSar) from ≈ 24 to 48 km; iv) the first guess (chosen here as the Bedmap 2 value h_b).

Remark 1 Using the explicit expression (2) of γ one can compute a-posteriori estimations of the (spatially distributed) slip ratio value R_s . This is an interesting feature to analyse a-posteriori the degree of the RU-SIA flow model consistency. The few a-posteriori analysis made (not presented here) remarkably confirms the good consistency of RU-SIA model.

Remark 2 Based on a-priori vertical thermal profile(s) (e.g. the one defined by (6)), the RU-SIA equation (1) provides a-posteriori estimations of the effective thermal boundary layer thickness $(B - b)$, see Fig. 2 (Left). Such a-posteriori estimations may be interesting for various analyses. Moreover the vertical profiles could be adjusted by constraining them with (the very few) in-situ measurements.

2.3.2 Details of Step 2): the Neural Network Residual Kriging (NNRK) algorithm

The employed NNRK algorithm is decomposed in three steps as follows.

Step 2a) Considering the surface data $(H, \mathcal{S}, |\mathbf{u}_H|, \dot{a}_b)$ at all in-situ measurements locations (e.g. along the flights tracks of all areas $Antp$) plus the values of γ_{tr}^* computed at Step 1), an estimator of γ is built up by training a ANN. This estimator is denoted by $\tilde{\gamma}$.

The training dataset is denoted by \mathcal{D} ; it contains "examples" (I_i, O_i) , $i = 1, \dots, N_{ft}$, where $I_i = (H, \mathcal{S}, |\mathbf{u}_H|, \dot{a}_b)(\mathbf{x}_i)$

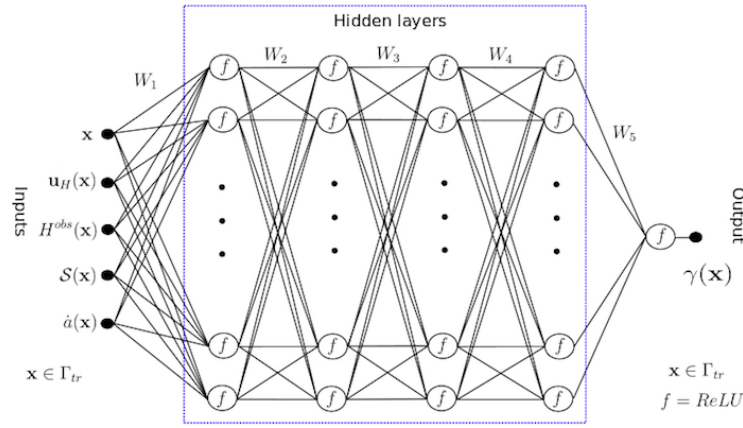


Fig. 3 The Artificial Neural Network (ANN) with four hidden layers. First step of the NNRK algorithm.

is the i -th input and $O_i = \gamma_{tr}^*(\mathbf{x}_i)$ is the corresponding output. \mathbf{x}_i , $i = 1, \dots, N_{ft}$ denote the i -th in-situ measurements coordinates (e.g. along the flight tracks).

The estimator $\bar{\gamma}$ is computed as the minimizer of the mean square misfit: $\frac{1}{N_{ft}} \sum_{i=1}^{N_{ft}} (O_i - \bar{\gamma}(I_i))^2$. This misfit function (also called loss function) reads:

$$j(\mathcal{D}; \cdot) = \frac{1}{N_{ft}} \sum_{i=1}^{N_{ft}} [\gamma_{tr}^*(\mathbf{x}_i) - \bar{\gamma}((H, \mathcal{S}, |\mathbf{u}_H|, \hat{a}_b)(\mathbf{x}_i); \cdot)]^2 \quad \text{for } \mathbf{x}_i \in \Gamma_{tr} \quad (10)$$

To solve this large dimensional data-based optimisation problem, the currently most efficient methods are ANN with few hidden layers (deep learning). Here, 5 layers are considered, see Fig. 3; each of the 4 hidden layers contains 50 neurons. The most efficient activation function is chosen: the rectified linear unit (ReLU) function, see e.g. [16, 32]. The ANN is determined by its architecture and the weight parameters (W_1, \dots, W_5) , Fig. 3.

The training step consists of identifying the optimal values of these parameters W_j , $j = 1, \dots, 5$. Each W_j is a matrix of dimension $n_{out} \times n_{in}$. Here, W_1 has $5 \times 50 = 250$ parameters, W_j for $j = 2, 3, 4$ have $50 \times 50 = 2500$ parameters each, W_5 has $50 \times 1 = 50$ parameters. The ANN has been coded in Python using the PyTorch and Mpi4Py libraries [10].

To minimize $j(\mathcal{D}; (W_1, \dots, W_5))$ with respect to $\{W_j\}_j$, the classical Adam method [31], a first-order gradient-based stochastic optimization, is employed. The learning rate (the gradient descent step size) is classically adjusted during the optimization procedure.

The input variables are heterogeneous and of different order of magnitude e.g. the elevation H (m) and the slope \mathcal{S} (radian). Therefore each input variable v , v an element of $\{H, \mathcal{S}, |\mathbf{u}_H|, \hat{a}_b\}$, are reduced centred as follows: $\bar{v}_i = (v_i - \text{mean}(v)) / \sigma(v)$, for all i , $1 \leq i \leq N_{ft}$. The normalisation is applied to mini-batches in hidden layers; this technique is supposed to improve the stability of the model; see e.g. [30] for more details and know-hows on ANN and NNRK algorithms.

Also to avoid overfitting, the dropout method [50] is adopted. (This technique may help to prevent overfitting). As usual, the hyper-parameters of the algorithm (learning rate, decay rate, dropout probability) are experimentally chosen; the selected values are those providing the minimal value of j .

The ANN has been trained by including h_b as an input parameter or not. Both estimators (considering h_b as an input or not) turned out to have similar accuracies; thus confirming the strategy to predict the dimensionless parameter γ of the flow model from the surface data only.

Step 2b) The K-fold cross-validation method, see e.g. [1], is employed to assess the ANN accuracy and to confirm if the ANN can be used as a predictor. Let us recall that K-fold cross-validation method is as follows, see e.g. [1]:

- Divide randomly the original training data set \mathcal{D} into K (roughly equal) subsets;
- For each subset \mathcal{D}_k , $k = 1 \dots K$, the ANN is trained from the other $(K - 1)$ subsets \mathcal{D}_i , $i \neq k$.

We denote by $\mathcal{D}_{i_{test}} = \mathcal{D}_i$ and $\mathcal{D}_{i_{train}} = \cup_{j \neq i} \mathcal{D}_j$, $i = 1, \dots, K$.

- Compute the loss function $j(\mathcal{D}_{i_{test}})$ for each case.

Finally, choose the best ANN i.e. those providing the smallest total loss function $j(\mathcal{D}_{i_{test}}) + j(\mathcal{D}_{i_{train}})$.

Step 2c) The residual at the measurements locations is computed: $\varepsilon_\gamma = (\gamma_{tr}^* - \bar{\gamma})$ with $\bar{\gamma}$ computed by the (best) ANN.

Next an ordinary Kriging (with a spherical semi-variogram model) is used to extend ε_γ all over the domain. The

obtained estimator is denoted by $\hat{\varepsilon}_\gamma$. By construction this residual satisfies: $\mathbb{E}(\varepsilon_\gamma) \approx 0$. Moreover the correlation between two points depends on the distance between them and not on their location. Performing an ordinary Kriging on the residual after ANN is known to be particularly efficient, see e.g. [30] Chapter 3.

The final estimator in the whole domain is denoted by $\hat{\gamma}$. It is obtained as the sum of the ANN estimator and the ordinary Kriging estimator of residuals:

$$\hat{\gamma}(\mathbf{x}) = \bar{\gamma}(\mathbf{x}) + \hat{\varepsilon}_\gamma(\mathbf{x}) \quad \text{for } \mathbf{x} \in \Omega \quad (11)$$

The forthcoming numerical results show that the estimator $\hat{\gamma}(\mathbf{x})$ provides (surprisingly) very accurate values of the parameter γ from the surface data only (altimetry, InSAR and \dot{a}).

2.3.3 On the linked uncertainty between γ and h

In the inversion algorithm previously described, after Step 1), one has to separate the effects of the two unknown fields: the physical-based dimensionless parameter γ and the ice thickness h . The accuracy and robustness of each VDA process are demonstrated by the numerical experiments presented later, see also [39]. It will be demonstrated in next section that the NNRK algorithm is robust and accurate too. Then it can be assumed that: $\gamma^t h^t \approx \gamma^* h^*$; where the superscript $*$ denotes the optimal computed values while the superscript t denotes the (effective) true value. Let us denote: $e_\varphi = (\varphi^* - \varphi^t)/\varphi$. At order 1, one has:

$$e_h \approx -e_\gamma \quad (\text{where } \gamma \text{ does not tend to } 0) \quad (12)$$

In other words, Step 2) and Step 3) of the inversion algorithm propagates the error made on γ to h in the same order of magnitudes (in %).

Remark 3 *It would be straightforward to apply the same NNRK algorithm to directly estimate the thickness h all over the domain. However it seems definitively more consistent to estimate a dimensionless parameter of a flow model able to represent accurately the surface data, than to estimate the thickness data partially responsible only of the employed surface data. Following this idea of purely data-driven estimations, [9] had proposed an ANN trained and assessed on synthetic data generated by an ice flow model and geomorphic premises to estimate the bedrock elevation of four mountain glaciers.*

3 Data pre-processing

In the next sections, the algorithm is applied to 6 large areas in EAIS (ranging from 250268 to 439045 km^2); they are denoted by Ant p , $p = 1, \dots, 6$, see Fig. 4. These areas include the upstream areas of major ice-sheds; all of them respect the flow model domain of validity. The mean thickness value of Bedmap2 ([14]) ranges from 1822 to 2745 m, see tables 2-11 for details. The coordinates of the characteristic points defining each area ($\approx 100 - 150$ points per area, see Fig. 4) are available on the open source computational software DassFlow webpage².

Estimating more accurately the bed elevation in these areas may be interesting since global warming may threaten EAIS stability as mentioned e.g. in [13].

The correlations between the given variables (H^{obs} , $\|\mathbf{u}_H\|$, \mathcal{S} , \dot{a} , h_b) for all areas have been computed. It turns out that no significant linear correlation between the variables have been observed.

In this section, the method to smooth the surface data accordingly with the flow model domain of validity is presented; the definition of adequate numerical grids follows. Moreover since Bedmap2 values are considered as the reference values, the method to obtain these values is recalled.

3.1 Minimal wave length, surface data smoothing and numerical grids

The surface data $|\mathbf{u}_H|$ and H have to be defined at an adequate scale to be consistent with the shallow (long wave assumption) flow model (1); next providing a minimal wave length L^* (km) of the inversions. The RU-SIA equation is accurate as soon as $\varepsilon = \frac{[H]}{[L]} \lesssim 0.1$. (In other respect it is shown in [54] that the ice-sheet areas presenting surface velocity ranging in $\approx [5 - 100]$ m/y are accurately modelled by the SIA model as soon as the minimal wave length equals $\approx 10 - 12$ km in mean).

The mean value of the Bedmap2 ice thickness (denoted by \bar{h}_b) [14] in the 6 Ant p areas equals ≈ 2.7 km. In the considered

² Open-source computational software DassFlow: Data Assimilation for Free Surface Flows. Python version for 2D shallow generalised Newtonian fluids. INSA, University of Toulouse, CNES. www.math.univ-toulouse.fr/DassFlow.

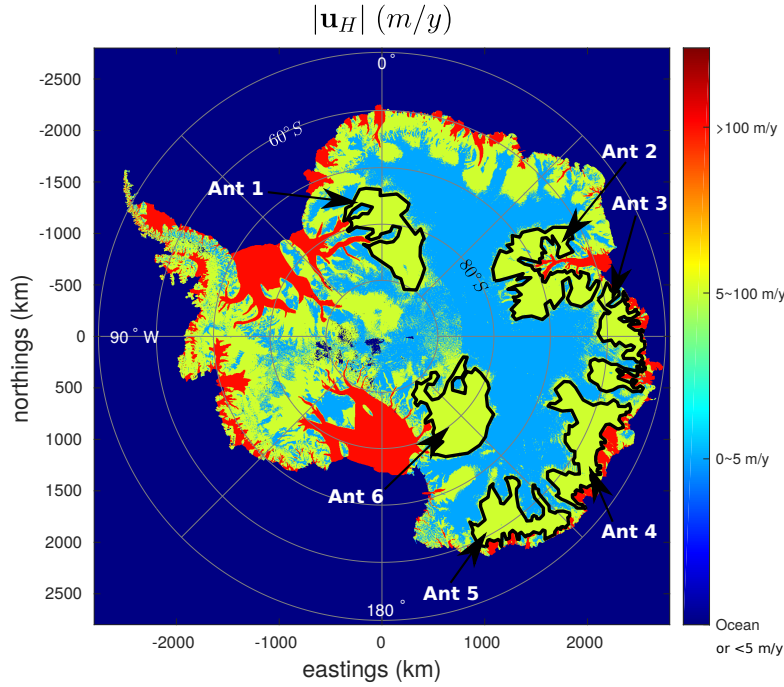


Fig. 4 Location of the 6 test areas Ant_p (east Antarctica) with InSAR-based surface velocity values in m/y (from [43]).

389 regimes, the velocity field is co-linear to the slopes \mathcal{S} ; therefore to be fully consistent, the smoothing of surface data
 390 should be done non-isotropically by defining a streamline minimal wave length and a cross-line one. For a sake of sim-
 391 plicity, here an isotropic smoothing is performed. To do so, a Gaussian with standard deviation $\sigma = 4$ km is convoluted
 392 with each given surface field: elevation and velocity norm. Then the smoothing effects are sensitive in disks of diameter
 393 $\approx 2 \times (3\sigma) \approx 10\bar{h}_b$ km.

394
 395 Next a finite element mesh is built up using Gmsh software [15] with a grid size $\delta x \approx 3$ km. Indeed $\delta x = 3$ km
 396 provides ≈ 10 points per minimal wave length L^* , therefore respecting the minimal number of points to properly approx-
 397 imate all fields. The flight tracks are meshed with cells of $\delta x \approx 2$ km. The given thickness measurements (provided in the
 398 Bedmap2 database [14]) are interpolated along the flight tracks .
 399

400 3.2 Recalls of the origins of Bedmap2 values

401 Bedmap2 values h_b are considered as reference values; moreover they are employed to set the first guesses of the VDA
 402 processes at Step 1) and Step 3) (see paragraph 2.3.2). h_b and its a-priori uncertainty as derived in [14] are plotted for each
 403 test area Ant_p in figures 6, 9, 12, 13, 14 and 15 (Middle)(Left). In Bedmap2 database [14], the interpolation - extrapola-
 404 tion of airborne measurements are performed throughout the domain by the ArcGIS Topogrid routine (ESRI Ltd, ArcGIS
 405 9); the latter is based on the ANUDEM algorithm [26]. This algorithm uses an iterative finite difference interpolation
 406 technique which is essentially a thin plate spline technique [53]. Next, empirical uncertainty values are stated as follows,
 407 see [14]. The thickness measurements are split into two datasets ($D1$) and ($D2$). Dataset ($D1$) is used to build up an inter-
 408 polation including at Dataset ($D2$) location points; values of ($D2$) being not used at this stage. Next, Dataset ($D2$) is used
 409 to quantify the misfit with the "predicted" - interpolated values; and basic statistics on the results with dependence on the
 410 distance to data are deduced. For cells located between 5 and 20 km from any data, [14] suggests that the interpolation
 411 error is an increasing function of distance from the closest data; beyond it would be not correlated. (Observe that this
 412 distance corresponds approximatively to the minimal wave length of the RU-SIA model). For cells that are more than 50
 413 km from airborne measurements, the thickness estimation is based on gravity-field inversion (gravity-derived thickness);
 414 the proposed related uncertainty equals $\pm 1000 m$. This is how the uncertainty values on Bedmap2 values h_b are defined;
 415 see figures 6, 9, 12, 13, 14 and 15 (Middle)(Right).

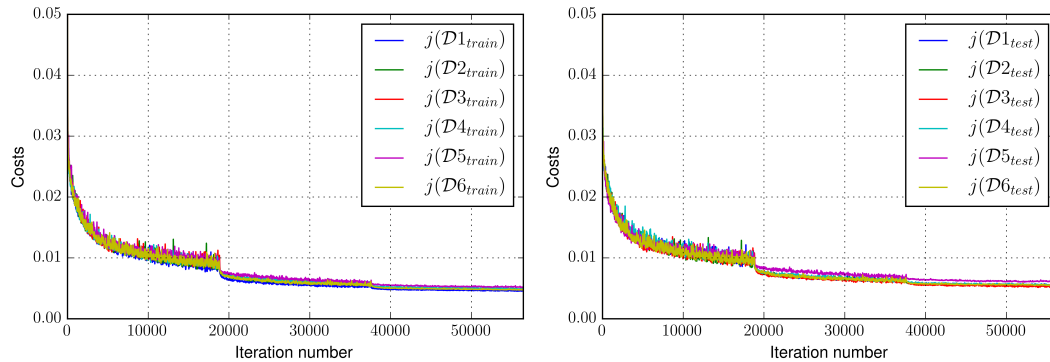


Fig. 5 Misfit functional $j(\mathcal{D})$ defined by (10), vs minimization iterations for: (Left) different train sets $\mathcal{D}_{i_{train}}$; (Right) different test sets $\mathcal{D}_{i_{test}}$. The learning rate (gradient descent step size) is decayed by 0.2 every 30 epochs (1 epoch = 1 forward pass and 1 backward pass of all the training examples), see e.g. [30] for details on this classical method.

4 Analysis of each inversion algorithm step

4.1 Step 1: Estimation of η by VDA

The effective diffusivity η defined in (1) is estimated in each area Ant_p by VDA following Step 1) described in Paragraph 2.3.1. The convergence of this iterative VDA process is very slow (a few hundreds of iterations) but very robust in particular with respect to the first guess value. This step has been thoroughly assessed in [39]. The stopping criteria is the stationarity of $\|\eta\|$. Here the RHS \dot{a} provided by [52] is supposed to be exact. After convergence of the VDA process, given the ice thickness along the flights tracks, the computed optimal value γ^* is saved for Step 2), that is:

$$\gamma_{tr}^*(\mathbf{x}) = \frac{\eta^*(\mathbf{x})}{h_b} \text{ for } \mathbf{x} \in \Gamma_{tr}$$

4.2 Step 2: Estimation of γ by NNRK

The ANN algorithm input values, see Fig. 3, are datasets along all flight tracks in all test areas Ant_p , $p = 1, \dots, 6$ plus the values of γ_{tr}^* computed at Step 1). This dataset is denoted by \mathcal{D} . Following Step 2b) (see paragraph 2.3.2), the K -fold cross-validations are performed with $K = 6$. The results are presented in Fig. 5. (The value $K = 6$ is completely independent of the total test cases number). Here, the training sets $\mathcal{D}_{i_{train}}$ contains 16774 examples and a test set $\mathcal{D}_{i_{test}}$ contains 3354 examples; each example being an (input, output) pair of ANN.

It can be read on Fig. 5 (Left) that all ANN models trained from the different data sets $\mathcal{D}_{i_{train}}$ provide very close cost values $j(\mathcal{D}_{i_{train}})$ (see (10)). Moreover, the cost values of all test sets $j(\mathcal{D}_{i_{test}})$ are almost all equal. This shows that all ANN have very close prediction capability, all being excellent. Indeed after optimisation, $j(\mathcal{D}_{i_{test}}) \approx 5 \cdot 10^{-3}$ (Fig. 5 (Right)); this corresponding to $\approx 1\%$ of the mean value of $\bar{\gamma}$. The ANN trained from $\mathcal{D}_{2_{train}}$ is selected since having a slightly smaller misfit value ($j(\mathcal{D}_{i_{train}}) + j(\mathcal{D}_{i_{test}})$). These tests of prediction capabilities demonstrate the robustness and accuracy of the trained ANN.

Next, values of $\bar{\gamma}$ are predicted in the whole domains Ω_p , $p = 1, \dots, 6$ by performing the selected ANN.

Next by performing the Kriging step (Step 2c) described in Paragraph 2.3.2), the predictor $\hat{\gamma}$ is obtained.

Following the a-priori estimation derived in Section 2.2, the upper bound 0.9 is imposed to the estimation; this upper bound is active at very few locations only; moreover it is in great majority where the uncertainty on h_b is low.

For each test area, the predicted values of γ are plotted; see figures 6, 9, 12, 13, 14 and 15 (Up) (R).

4.3 Step 3: Estimation of h (and adjustment of \dot{a}) by VDA

After Step 2), the dimensionless parameter γ in RU-SIA equation (1) is given. Then the thickness h is inferred by VDA following the method presented in paragraph 2.3.1. The optimisation algorithm converges in $\sim 20 - 50$ iterations depending on the test case. Its convergence is robust; this point has been thoroughly analysed in [39].

At this step, h is simultaneously inferred with \dot{a} . Indeed this enables to adjust the value of \dot{a} within its uncertainty range which is here $\sim \pm 20\%$, see [52]. It can be noticed in tables 2, 5, 8, 9, 10 and 11 that the corrections made remains in great part within this a-priori uncertainty range. Indeed the upper bound is active at few locations only. In other words, this adjustment based on the physical-based model RU-SIA is consistent with the (totally independent) estimations derived

Table 1 Difference between values of H the response of RU-SIA equation (1) if changing the RHS value: \hat{a}_b the Racmo2 value, \hat{a}^* the inferred value at Step 3). Domain $\Omega_p = \text{Ant1}$.

Difference of H	Median	Mean	Max
$ H(\hat{a}_b) - H(\hat{a}^*) $	3.3m	6.0m	26.3m

445 in [52].

446 Of course, given the surface data, any change of \hat{a} in RU-SIA equation (1) has an effect on the inferred value of h . As an
 447 example let us compute the response H of RU-SIA equation (1) in Ant1 area with: i) the RACMO2 value \hat{a}_b in the RHS
 448 (providing $H(\hat{a}_b)$); ii) the inferred value \hat{a}^* by VDA in the RHS (providing $H(\hat{a}^*)$). The obtained difference are the ones
 449 indicated in Tab. 1. Therefore the correction made on the RHS $\hat{a} = (\partial_t h - a)$ implies a correction on the ice thickness
 450 h negligible ($\sim 1\%$) compared to the one obtained by the complete inversion method, see Tab. 2 in next section. This
 451 remark holds for all the domains Ω_p .

452

453 4.4 On the RU-SIA model accuracy

454 For each test area Ant_p , domain information and basic statistics on the results are presented, see tables 2, 8, 5, 9, 10, 11.
 455 Statistics on the computed surface elevation H , output of RU-SIA model, are indicated. It can be noticed that the RU-SIA
 456 equation solved from Bedmap2 value h_b and the (purely data-driven) estimation of γ obtained at Step 2) already fits very
 457 well the measured surface elevation H^{obs} , see "Direct model validation" lines in the tables. This very good accuracy
 458 (based on the Bedmap2 bed elevation h_b i.e. without any additional calibration of h) demonstrates the validity and the
 459 relevance of the RU-SIA model. After Step 3) of the inversion algorithm i.e. after the identification of h and \hat{a} by VDA,
 460 of course the RU-SIA model fits even better the measured surface elevation H^{obs} , see " $|H(h^*) - H^{obs}|$ (after h -inversion)"
 461 in the tables.

462

463 5 Results and sensitivity tests (Ant1 and Ant3 areas)

464 In this section, the bed elevation b (equivalently the ice thickness h) is inferred by the inverse method described in Section
 465 2.3 for the two areas Ant1 and Ant3, see Fig. 4, tables 2 and 5. Different estimations of h are compared, depending if:

- 466 a) isolated flight tracks (hence locally highly constraining) are considered or not;
- 467 b) the learning method at Step 2) is the NNRK algorithm described in Paragraph 2.3.2, or an ordinary Kriging method
 468 like it is done in [39].

469 These comparisons aim at analysing the robustness and accuracy of the present inverse method.

470 Ant1 is a 370809 km² area north-east upstream of Bailey, Slessor and Recovery ice-streams; Ant3 is a 250268 km² area
 471 in Wilhelm and Queen Mary lands, upstream of Shackleton ice shelf and Davis sea.

472 Among the considered six areas, Ant1 and Ant3 are those presenting the largest uncovered parts during airborne cam-
 473 paigns. As a consequence they contain large areas where Bedmap2 estimation h_b is based on gravity field inversions,
 474 therefore presenting very large uncertainties.

475 For each case, the domain information and basic statistics on the numerical results are presented in tables 2 and 5. For
 476 each case, the most relevant fields are plotted, see figures 6 and 9: the surface velocity norm $|\mathbf{u}_H|$ and the flight tracks lo-
 477 cations (Up)(L), the NNRK estimation $\hat{\gamma}$ defined by (11) (Up) (R), the Bedmap2 value h_b (Middle)(L) with its uncertainty
 478 as presented in [14] (Middle)(R), the present thickness estimation h^* (Down)(L) and its difference with h_b (Down)(R).

479 5.1 Results for Ant1 area

480 This domain presents large unexplored areas during the airborne campaigns therefore huge uncertainty on h_b values, see
 481 Fig. 6 (Middle).

482 5.1.1 The ice thickness estimation h^*

483 Recall that $\hat{\gamma}$ is the NNRK estimation of the dimensionless parameter γ defined by (2). No correlation is observed between
 484 h and γ ; the only clearly observed correlation is : γ is small where $|\mathbf{u}_H|$ is small, see Fig. 6 (Up). This observation is fully
 485 consistent with the a-priori analysis done in Section 2.2, see (2) and Fig. 2.

486 Recall that h_b values are thin plate spline based estimations (see [14] and paragraph 3.1) hence intrinsically smooth, Fig. 6

Table 2 Domain Ω_p =Ant1, information and results.

Domain Ω_p & mesh information				
Surface $ \Omega_p $	370809 km^2			
Mean ice thickness of h_b (Bedmap2)	2696.2 m			
# mesh vertices: in Ω_p / on flight tracks	57661 / 2152			
RU-SIA model output (with $\hat{\gamma}$)		Median	Mean	Max
$ H(h_b) - H^{obs} $ (before h -inversion)		7.0 m	10.3 m	53.0 m
$ H(h^*) - H^{obs} $ (after h -inversion)		2.6 m	3.7 m	44.6 m
Infered RHS \dot{a}				
$ \dot{a}^* - \dot{a}_b $		0.7 cm/y	0.7 cm/y	3.6 cm/y
$ \dot{a}^* - \dot{a}_b / \dot{a}_b $		19.2 %	17.0 %	20.0 %
Infered thickness h				
$ h^* - h_b $		275.2 m	356.8 m	1953.5 m
$ h^* - h_b / h_b $		10.4 %	13.3 %	65.7 %
Ice volume change in km^3 / in %		1.6 $10^4 km^3$ / 1.6 %		

487 (Middle)(Left). The present estimation h^* is the optimal solution of a data-driven model combined with a physical-based
 488 model; no additional smoothing has been added, then the obtained value h^* is much less smooth than h_b . It is worth to
 489 notice that a non isotropic smoothing of the surface data (see the previous section) would have provided bed elevation
 490 patterns more correlated to the surface streamlines.

491 The difference between h^* and h_b is not correlated to the distance to the nearest h measurement (flight track), on contrary to
 492 the empirically stated uncertainty in [14]. Indeed large corrections of h_b (up to 1500 m) are obtained close to flight tracks;
 493 close meaning at 1 – 2 minimal wave lengths of the RU-SIA model that is $\sim 20 - 40$ km, see e.g. in Fig. 6 (Down)(R) the
 494 areas around coordinates (2750,1950)(2900,1550)(3050,2050). At the opposite, h^* may remain very close to h_b in areas
 495 relatively far from any flight tracks.

496 Recall that the flight tracks are meshed as 1d lines; along these segments (≈ 2 km long), the infered depth value can
 497 vary of $\pm 150m$ around the measured values (inequality constraints imposed in the VDA processes). Therefore in the
 498 adjacent triangles (which are nearly equilateral with ≈ 2 km edges), the plotted mean depth values may be already much
 499 different than the measured ones. This large scale smoothing may explain the potential great differences between the two
 500 estimations even relatively close to the flight tracks.

501 The basic statistics presented in Tab. 2 show that after the VDA processes, the RU-SIA equation fits extremely well the
 502 measured surface elevation. The correction made on \dot{a} is relatively consequent, 17% in mean (it is the highest correction
 503 made among the 6 test cases Ant p). However it remains lower than the maximal authorised correction: $\pm 20\%$.

504 Finally the correction made on h_b is non negligible: 13.3% (356.8 m) in mean, with a 1.6% ($1.6 \cdot 10^4 km^3$) of volume
 505 change only (for 370809 km^2).

506 5.1.2 Ant1: if removing some flight tracks

507 In this paragraph, a new ice thickness estimation is computed. It differs from h^* since the flight tracks indicated in
 508 Fig.6 (Up)(L) are not considered anymore. The original complete set of flight tracks is denoted by Γ^{all} ; the partial one
 509 is denoted by Γ^{less} . In Γ^{less} case, the mesh of the entire area has been re-built (since in each mesh, the lineaic flight
 510 tracks are meshed differently). The inverse problem based on Γ^{less} is less constrained in particular the two VDA processes
 511 (Steps 1 and 3). Indeed the removed flight tracks are isolated, see Fig. 6(Up)(L); no constraint is imposed in the vicinity
 512 of these removed flight tracks anymore.

513 The statistical learning at Step 2) is unchanged, therefore values of $\bar{\gamma}$ are unchanged too. However the estimation $\hat{\gamma}$
 514 defined by (11) is not the same since the Kriging step is changed. Indeed the latter is based on less flight tracks data.
 515 The difference between the two estimations ($\bar{\gamma}(\Gamma^{all}) - \hat{\gamma}(\Gamma^{less})$) is plotted in Fig. 7 (Up)(R). It can be noticed that $\hat{\gamma}$
 516 is changed all over the domain and not particularly in the vicinity of the missing flight track. Indeed, the Kriging method
 517 (Step 2c) in Paragraph 2.3.2) aims at computing the minimal variance in norm 2 (least square) and not point-wise; hence
 518 the global change of $\hat{\gamma}$.

519 Next the infered thickness h^* is different for two reasons: 1) values of γ are different; 2) the VDA process of Step 3)
 520 is not locally constrained at the missing flight tracks locations. The difference between the two thickness estimations is
 521 plotted in Fig. 7 (Down)(R). For a sake of readability, the legend in Fig. 7(Down)(R) has been bounded at $\pm 400m$ (very
 522 few locations were greater than this bound). Basic statistics on the difference are presented in Tab. 3. Differences of 300
 523 m correspond to $\approx 10 - 15\%$ of change. As expected, see (12), the variations of h are correlated to the variations of γ :
 524 compare Fig. 7 (Up)(R) to (Down)(R). Since the global change of γ , the change of h is not particularly important around
 525 the missing flight tracks.

526 Finally, it is worth to mention that the present inversion method is relatively global with local constraints ("in-situ"
 527 measurements along the flight tracks); it is not purely local inversions. In the present experiment, the obtained variations

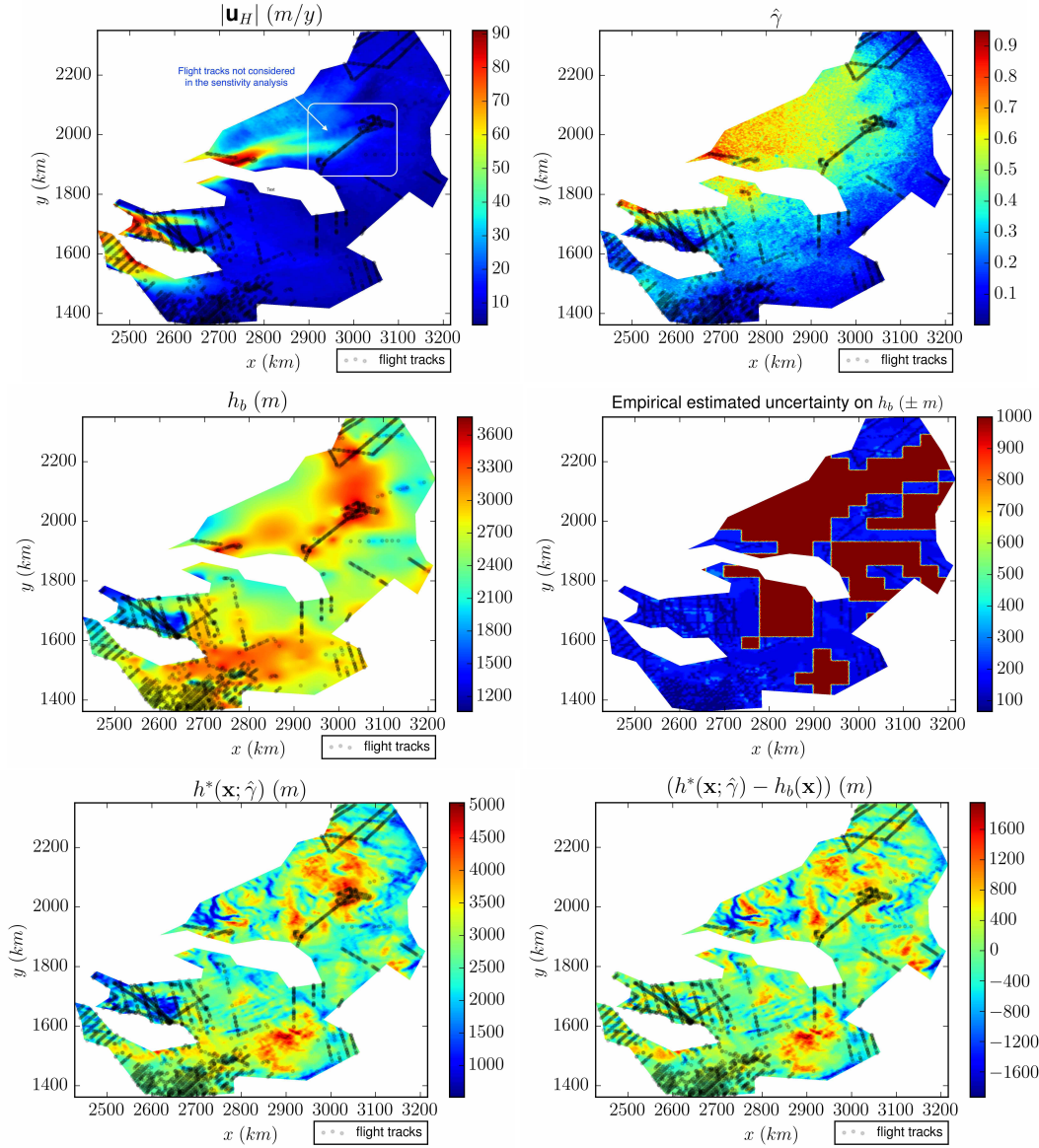


Fig. 6 Domain $\Omega_p=Ant1$ (the plotted coordinates equal the Eastings-Northings plus (2800, 2800)km): (Up)(L) Surface velocity module $|u_H|$ and flight tracks (R) $\hat{\gamma}$ computed by NNRK, see (11). (Middle)(L) Thickness h_b from Bedmap2 [14] (R) Empirical uncertainty on h_b from [14]. (Down)(L) Inferred thickness with $\hat{\gamma}$: $h^*(\hat{\gamma})$ (R) Difference $(h^*(\hat{\gamma}) - h_b)$.

Table 3 Domain $\Omega_p=Ant1$. Comparison of the estimations if considering or not the flights tracks indicated in Fig.6 (Up)(L).

Inferred thickness difference	Median	Mean	Max
$ h^*(\Gamma_{ir}^{all}) - h^*(\Gamma_{ir}^{less}) $	151.3 m	196.9 m	1524.5 m
$ h^*(\Gamma_{ir}^{all}) - h^*(\Gamma_{ir}^{less}) / h^*(\Gamma_{ir}^{less}) $	5.6%	6.6%	80.0%

528 of h^* are roughly half of the ones obtained from h_b , see tables 2 and 3: difference of 6.6% in mean vs 13.3%, and 5.6%
 529 vs 10.4% for median values.

530 5.1.3 Ant1: with a different statistical learning method at Step 2)

531 It has been previously shown that uncertainties on γ generates uncertainties on h of same order of magnitude, see (12). In
 532 this paragraph, the influence of the statistical estimator considered at Step 2) is investigated. To do so, first we compare:

- 533 a) $\bar{\gamma}$ obtained by ANN algorithm at Step 2a) to $\hat{\gamma}$ obtained by the complete NNRK algorithm (see (11));
- 534 b) γ_{krig} obtained by an ordinary Kriging of values inferred along the flights tracks to $\hat{\gamma}$.

535 It may be a-priori guessed that a deep learning method (as the present NNRK algorithm) is more reliable than a
 536 Kriging inter/extrapolation of its values between the flight tracks.

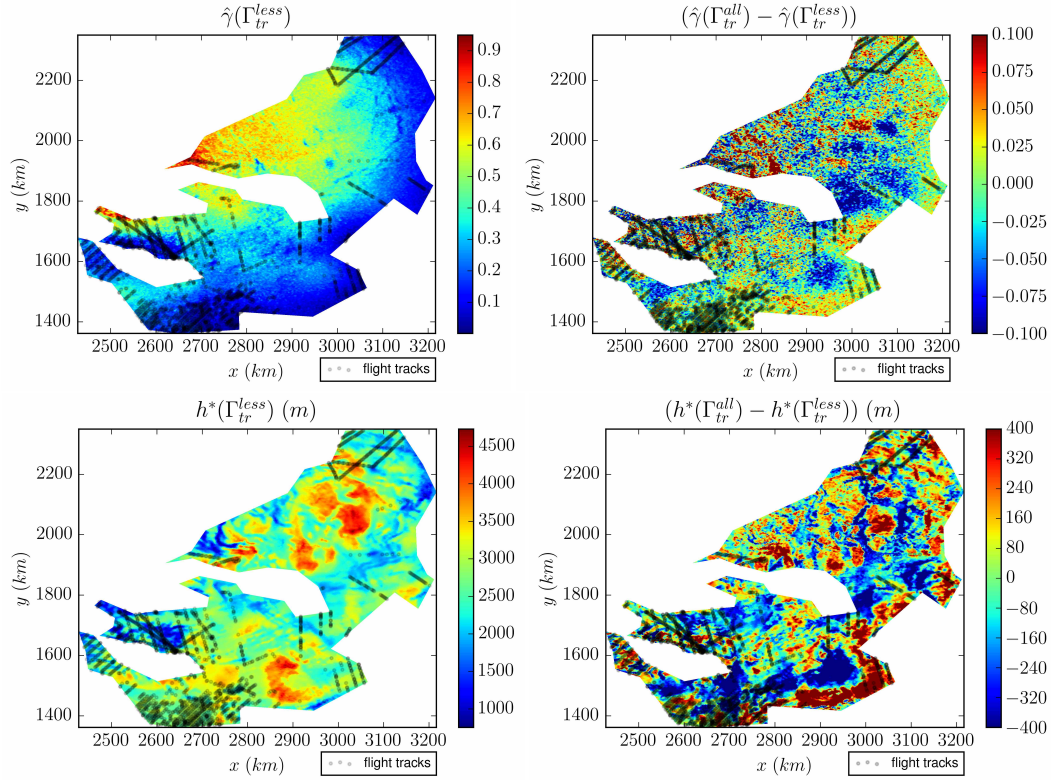


Fig. 7 Domain Ω_p =Ant1: comparison if not considering the flights tracks indicated in Fig.6 (Up)(L). (Up)(L) Field $\hat{\gamma}(\Gamma_{tr}^{less})$ (i.e. without the flights tracks indicated in Fig.6 (Up)(L)). (R) Difference $(\hat{\gamma}(\Gamma_{tr}^{all}) - \hat{\gamma}(\Gamma_{tr}^{less}))$. (Down)(L) Inferred thickness $h^*(\Gamma_{tr}^{less})$ (R) Difference between the two estimations: $(h^*(\Gamma_{tr}^{all}) - h^*(\Gamma_{tr}^{less}))$.

Table 4 Domain Ω_p =Ant1. Comparison the original thickness estimation (obtained using NNRK) to the one obtained using ordinary Kriging at Step2)

Inferred thickness difference	Median	Mean	Max
$ h^*(\hat{\gamma}) - h^*(\gamma_{krig}) $	145.5 m	183.5 m	1264.2 m
$ h^*(\hat{\gamma}) - h^*(\gamma_{krig}) / h^*(\hat{\gamma}) $	5.3%	7.2%	117.2%

537 Second, we compare the inferred thickness h^* obtained from $\hat{\gamma}$ (that is the original estimation plotted in Fig. 6
538 (Down)(L)) to the one obtained from γ_{krig} .

539
540 As expected, the difference between $\bar{\gamma}$ and $\hat{\gamma}$ (i.e. before and after the Kriging Step 2c) are localised in the vicinity
541 of the flight tracks. In Ant1 case, these differences may be up to $\sim \pm 20\%$, see Fig. 8(Up)(R). More interestingly and as
542 expected too, the differences between $\hat{\gamma}$ and γ_{krig} are not clearly correlated to the distance to the nearest flight track. The
543 observed difference in Ant1 case may be consequent: $\sim \pm 40\%$, see Fig. 8(Middle)(R).

544 Next, like in the previous sensitivity test (and for the same reasons), the variations of h are correlated to the variations
545 of γ : compare Fig. 8 (Middle)(R) to (Down)(R). Some statistics on the differences are presented in Tab. 4. Again the
546 obtained variations in h are roughly half of the ones obtained from h_b , see tables 2 and 4: difference of 7.2% in mean vs
547 13.3%, and 5.3% vs 10.4% for median values.

548

549 5.2 Results for Ant3 area

550 Like Ant1, Ant3 area presents large uncovered areas during the airborne campaigns, corresponding to huge uncertainty
551 on h_b , see Fig. 9.

552 5.2.1 The ice thickness estimation h^*

553 Like in Ant1 case, the only observed correlation is: γ is small if \mathbf{u}_H is small, see Fig. 9 (Up). Again the difference between
554 h^* and h_b is uncorrelated to the distance to the nearest flight track (on contrary to the empirically established uncertainty
555 in [14]). Large corrections of h_b (up to 700 m) are found close to flight tracks see e.g. the area around coordinates
556 (5550,2800) in Fig. 6 (Down)(R); at the opposite, h^* may remain very close to h_b in areas relatively far from any flight

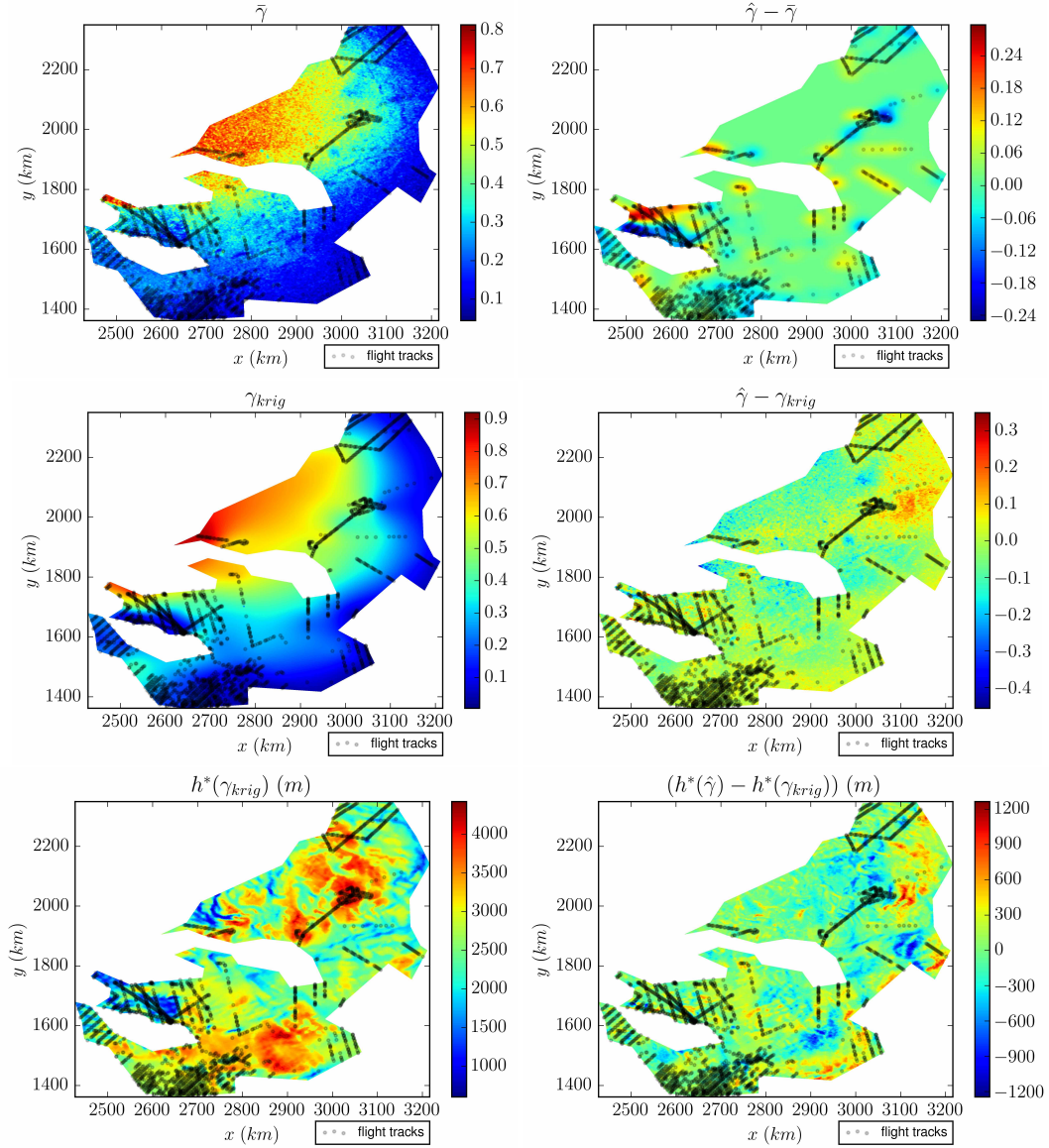


Fig. 8 Domain $\Omega_p = \text{Ant1}$: comparison between different statistical learning methods at Step 2. (Up)(L) $\hat{\gamma}$ computed by ANN only. (R) Difference $(\hat{\gamma} - \tilde{\gamma})$. (Middle)(L) γ_{krig} computed by ordinary Kriging. (R) Difference $(\hat{\gamma} - \gamma_{krig})$. (Down)(L) Inferred thickness $h^*(\gamma_{krig})$. (R) Difference $(h^*(\hat{\gamma}) - h^*(\gamma_{krig}))$.

557 tracks, see e.g. the area around coordinates (5250,2800).

558 The few statistics presented in Tab. 5 show that again after the VDA processes, the RU-SIA equation fits extremely
 559 well the measured surface elevation. The correction made on \hat{a} is much lower than the authorised maximal variation:
 560 11.2% in mean. In Ant3, the global correction made on h_b is relatively low: 6.6% in mean (3.5% median) with a 0.5%
 561 of volume change only. However in the most uncertain areas, the corrections made can be either low, see e.g. the areas
 562 around coordinates (5000,2650) (5200,3250), or important ($\pm \sim 700\text{m}$), see e.g. the area around coordinates (5000,2650).

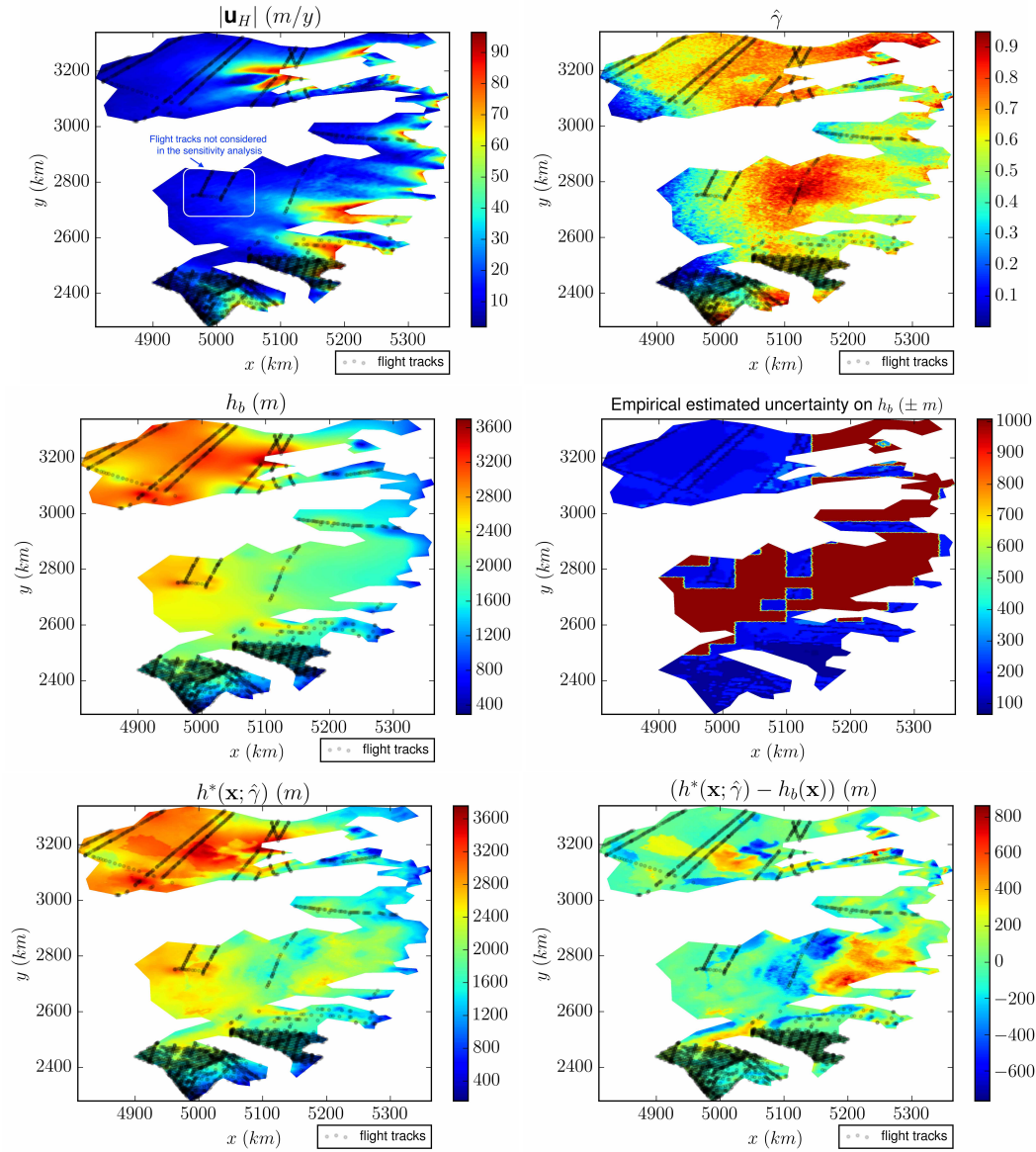
563

564 5.2.2 Ant3: if removing some flight tracks

565 The ice thickness obtained if not considering the flight tracks indicated in Fig.9 (Up)(L) is compared to the original
 566 estimation h^* (the one plotted in Fig.9 (Down)(L)). For the same reason as in Ant1 case, both $\hat{\gamma}$ and h are changed all over
 567 the domain and in the vicinity of the missing flight track only. Largest changes are obtained in areas far to the missing
 568 tracks; also it may close to (assimilated) flight tracks, see e.g. the area around coordinates (5100,3200). The difference
 569 between the two estimations are plotted in Fig. 6 (Up)(R) and (Down)(R). (Again for a sake of readability, the legend
 570 in Fig. 10(Down)(R) has been bounded at $\pm 400\text{m}$; very few values being greater than this bound). Basic statistics on
 571 the difference are presented in Tab. 6. (A difference of 200m corresponds to $\approx 10\%$ of change). Again, the obtained

Table 5 Domain Ω_p =Ant3, information and results.

Domain Ω_p & mesh information				
Surface $ \Omega_p $	250268 km^2			
Mean ice thickness of h_b (Bedmap2)	1822.8 m			
# mesh vertices: in Ω_p / on flight tracks	42881/2443			
RU-SIA model output (with $\hat{\gamma}$)		Median	Mean	Max
$ H(h_b) - H^{obs} $ (before h -inversion)		7.8 m	12.7 m	274.0 m
$ H(h^*) - H^{obs} $ (after h -inversion)		2.8 m	4.0 m	110.6 m
Inferred RHS \dot{a}				
$ \dot{a}^* - \dot{a}_b $		2.2 cm/y	2.5 cm/y	22.1 cm/y
$ \dot{a}^* - \dot{a}_b / \dot{a}_b $		11.2%	11.4%	20%
Inferred thickness h				
$ h^* - h_b $		70.0 m	124.5 m	862.2 m
$ h^* - h_b / h_b $		3.5%	6.6%	63.5%
Ice volume change in km^3 / in %		3.0 $10^3 km^3$ / 0.5%		

**Fig. 9** Domain Ω_p =Ant3 (the plotted coordinates equal the Eastings-Northings plus (2800,2800)km): (Up)(L) Surface velocity module $|u_H|$ and flight tracks (R) $\hat{\gamma}$ computed by NNRK, see (11). (Middle)(L) Thickness h_b from Bedmap2 [14] (R) Empirical uncertainty on h_b from [14]. (Down)(L) Inferred thickness with $\hat{\gamma}$: $h^*(\hat{\gamma})$ (R) Difference $(h^*(\hat{\gamma}) - h_b)$.

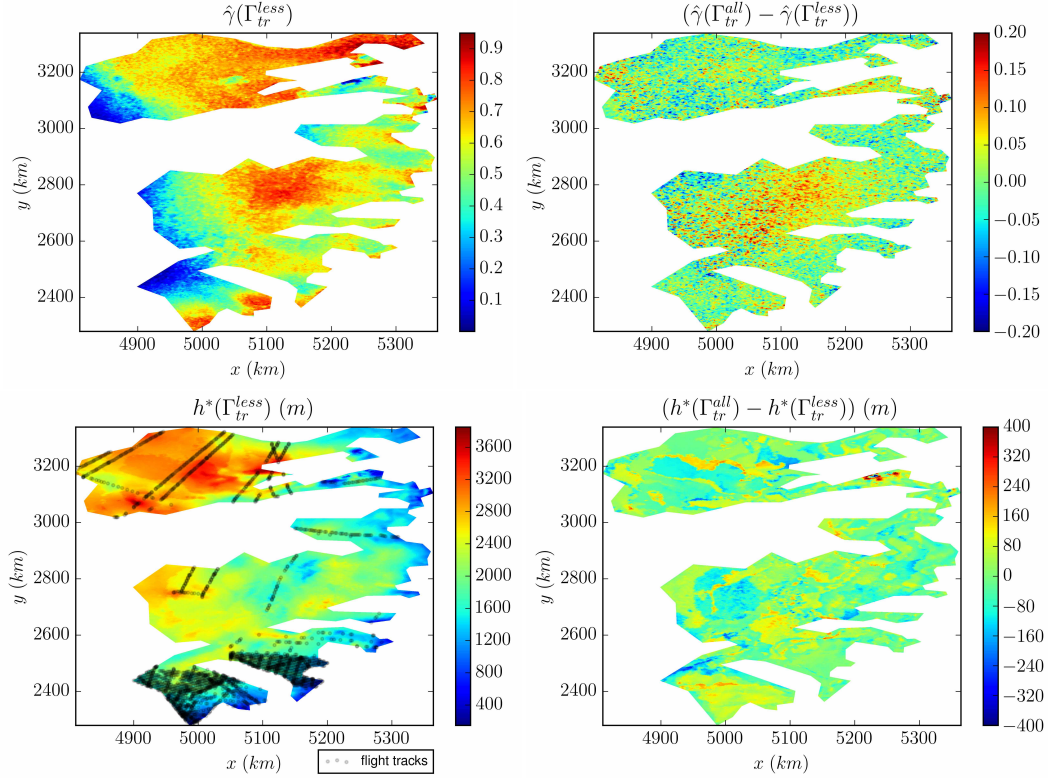


Fig. 10 Domain $\Omega_p=Ant3$: comparison if not considering the flights tracks indicated in Fig.9 (Up)(L). (Up)(L) Field $\hat{\gamma}(\Gamma_{tr}^{less})$ (i.e. without the flights tracks indicated in Fig.9 (Up)(L)). (R) Difference $(\hat{\gamma}(\Gamma_{tr}^{all}) - \hat{\gamma}(\Gamma_{tr}^{less}))$. (Down)(L) Inferred thickness $h^*(\Gamma_{tr}^{less})$. (R) Difference between the two estimations: $(h^*(\Gamma_{tr}^{all}) - h^*(\Gamma_{tr}^{less}))$.

Table 6 Domain $\Omega_p=Ant3$. Comparison if considering or not the flights tracks indicated in Fig.9 (Up)(L).

Inferred thickness difference	Median	Mean	Max
$ h^*(\Gamma_{tr}^{all}) - h^*(\Gamma_{tr}^{less}) $	42.7 m	56.3 m	904.6 m
$ h^*(\Gamma_{tr}^{all}) - h^*(\Gamma_{tr}^{less}) / h^*(\Gamma_{tr}^{less}) $	2.2%	2.8%	78.7%

Table 7 Domain $\Omega_p=Ant3$. Comparison of the original thickness estimation (obtained using NNRK) to the one obtained using ordinary Kriging at Step2).

Inferred thickness difference	Median	Mean	Max
$ h^*(\hat{\gamma}) - h^*(\gamma_{krig}) $	58.3 m	84.9 m	1418.7 m
$ h^*(\hat{\gamma}) - h^*(\gamma_{krig}) / h^*(\hat{\gamma}) $	2.9%	4.3%	124.5%

572 variations on h are roughly half than the ones obtained from h_b , see tables 5 and 6: difference of 2.8% in mean vs 6.6%,
 573 and 2.2% vs 3.5% for median values.

574 5.2.3 Ant3: with a different statistical learning method at Step 2)

575 Similarly to the Ant1 case, the difference between $\bar{\gamma}$ and $\hat{\gamma}$ (i.e. before and after the Kriging Step 2c) are mainly localised
 576 in the vicinity of the flight tracks with amplitudes up to $\sim \pm 0.20$, Fig. 11 (Up)(R). Again, the differences between $\hat{\gamma}$ and
 577 γ_{krig} are not in the vicinity of the tracks only; they may be anywhere. The observed difference is up to $\sim \pm 0.45$, see
 578 Fig. 11(Middle)(R). Statistics on the differences on the corresponding estimated thicknesses are presented in Tab. 7. The
 579 obtained differences on h are about one third lower than the ones obtained from h_b , see tables 2 and 7: difference of 4.3%
 580 in mean vs 6.6%, and 2.9% vs 3.5% for median values.

581
 582 In summary, these empirical sensitivity analyses highlight the robustness and the reliability of the inversion method.
 583 If not considering some in-situ measurements (along some flight tracks), see figures 6 and 9 (Up)(L), the obtained differ-
 584 ences on h are roughly half than the ones obtained between h^* and h_b .
 585 If considering a simple Kriging method to estimate γ instead of the NNRK algorithm, the obtained differences on h in
 586 Ant1 case (resp. in Ant3 case) are roughly 1/2 (resp. 2/3) the ones obtained between h^* and h_b .
 587 Therefore in all investigated cases, the obtained variations are lower than the ones obtained from h_b , see sections 5.1.1
 588 and 5.2.1.

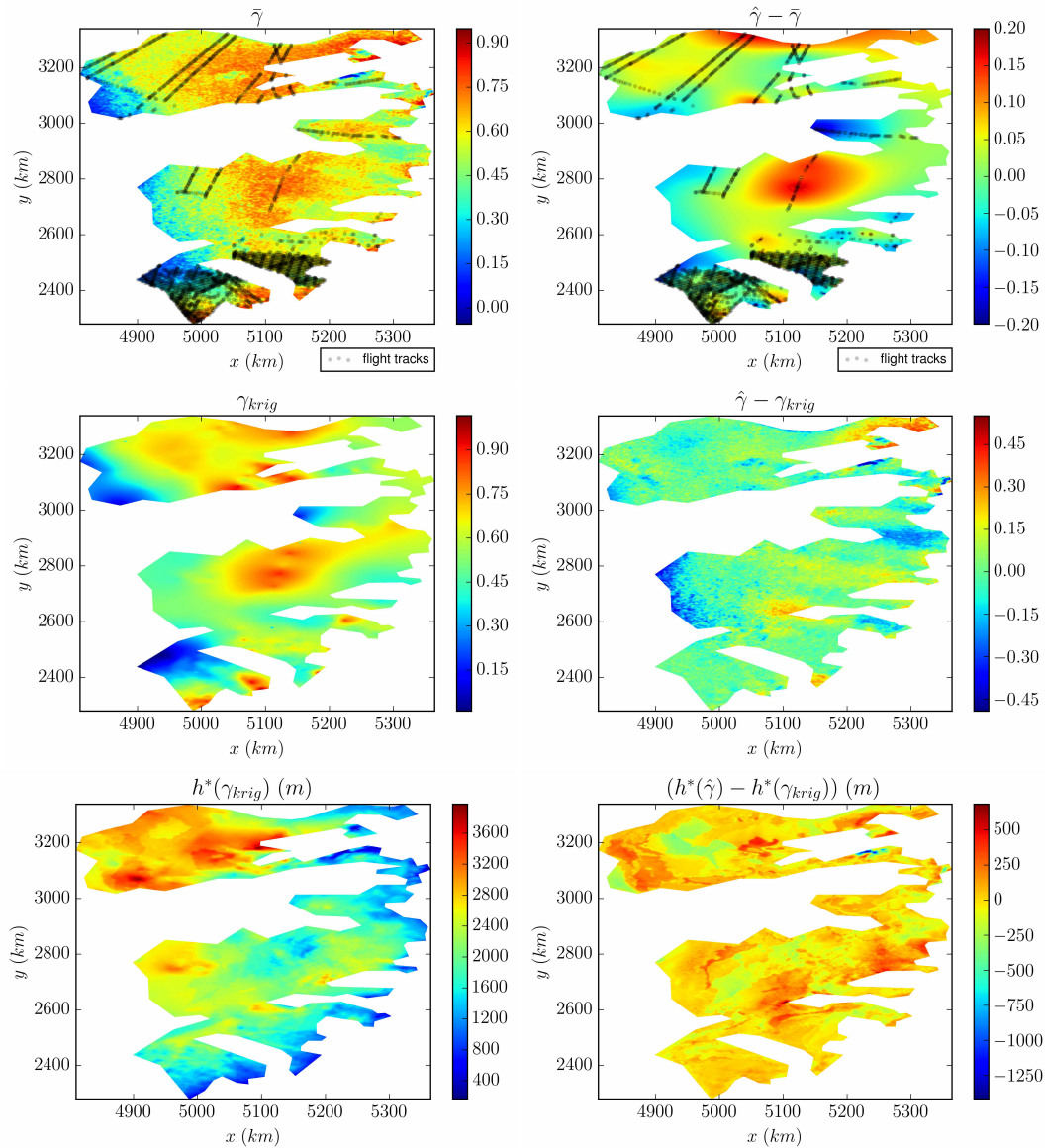


Fig. 11 Domain $\Omega_p = \text{Ant3}$: comparison between different statistical learning methods at Step 2). (Up)(L) $\hat{\gamma}$ computed by ANN only. (R) Difference $(\hat{\gamma} - \bar{\gamma})$. (Middle)(L) γ_{krig} computed by ordinary Kriging. (R) Difference $(\hat{\gamma} - \gamma_{krig})$. (Down)(L) Inferred thickness $h^*(\gamma_{krig})$. (R) Difference $(h^*(\hat{\gamma}) - h^*(\gamma_{krig}))$.

589 6 Conclusion

590 In this study, a method to infer the bedrock topography beneath glaciers at wave length $\sim 10\bar{h}$, \bar{h} a characteristic thick-
 591 ness value (with a resolution at $\sim \bar{h}$) is developed. The key ingredients of this inversion method are the following: a)
 592 a dedicated Reduced-Uncertainty flow model (RU-SIA) taking into account a complete physics (including non-uniform
 593 internal deformation in particular due to the temperature profile); the model presents a single dimensionless multi-physics
 594 parameter $\gamma(\mathbf{x})$; b) two advanced VDA processes; c) an Artificial Neural Network (ANN) estimating $\gamma(\mathbf{x})$ from the sur-
 595 face data and in-situ measurements (acquired during airborne campaigns). A strong feature of the method is to consider
 596 at each step robust and stable inverse problems (or at least not trivially ill-posed ones). All steps of the algorithm have
 597 been thoroughly assessed, partly in [39] next in the present study, in particular the estimation sensitivity with respect to
 598 the presence or not of local in-situ measurements (airborne campaigns). The ANN capabilities to infer the dimensionless
 599 multi-physics parameter γ from the surface measurements only are surprisingly excellent for all considered datasets in
 600 EAIS.

601 Observe that it is straightforward to apply the same deep-learning method as the present one to directly estimate the
 602 ice thickness h (instead of γ), by training the ANN from the in-situ measurements acquired along the flight tracks. We
 603 have performed such estimations; they turned out to be too highly dependent on the training datasets. In particular, they
 604 are sensitive to the presence or not of local in-situ measurements. In other words, these purely data driven estimations

605 turned out to be not robust enough, on contrary to the estimations of γ . It seems more consistent to estimate an "intrinsic"
 606 dimensionless multi-physics parameter from the surface signature than the ice depth.
 607 The present hybrid physically-informed data-driven method enables the estimation of the bed elevation between in-situ
 608 measurements, in poorly covered areas, even in large uncovered areas e.g. in EAIS where the current estimations are
 609 today gravimetry-based (therefore highly uncertain). Indeed, the developed method is relatively global (with local con-
 610 straints along the flight tracks) and not purely local. It has been shown to be relatively robust. The estimations in large
 611 uncovered areas remain accurate as elsewhere. In the considered six large EAIS areas, the corrections made to Bedmap2
 612 may be large (up to 1000m) even at 2 wave lengths ($\approx 50\text{km}$) away to "in-situ" measurements (flight tracks). Away from
 613 the flight tracks, the correction obtained to Bedmap2 may be significant or not, depending on the surface signature. The
 614 obtained corrections led to a total ice volume change of 0.5 – 5.6%, depending on the area.
 615 In view to edit new bedrock maps from the present estimation method, further investigation need to be led in particular
 616 by adding additional prior information such as regularisation length scales of h . In a mathematical point of view, this can
 617 be easily done (by adding extra regularisation terms in the optimisation formulations). This prior information should be
 618 introduced from geomorphologic analyses. Moreover, the smoothing of the observational surface term $|\mathbf{u}_H|/\mathcal{S}$ may be
 619 defined as non-isotropic to distinguish the streamline minimal wave length from the cross-line one.
 620 This bed estimation method may be applied to any ice-sheets or ice-caps, as soon as the method domain of validity is
 621 compatible with the observed flows, that is highly to moderately sheared flows (i.e. not almost purely slipping flows). Fi-
 622 nally, the method can be easily extended to unsteady flows if the surface observations (elevation and velocity) are given in
 623 time and assuming that the initial condition is either not important at the considered time scale or approximatively known.
 624

625 *Acknowledgments & Authors' contributions*

626 J.M. has defined the research plan, has derived the equations and the computational methods and has written the manuscript.
 627 J.Z. has written the computational code, has performed all the numerical results (plus many exploring ones). Both have
 628 analyzed the numerical results.
 629 J.Z. has been funded by a CNES TOSCA grant (oct. 2017-sept. 2018) during her post-doctoral stay at IMT - INSA
 630 Toulouse.
 631 J.M. acknowledges M. Morlighem (Univ. California of Irvine) and H. Seroussi (JPL/Caltech-NASA) for numerous dis-
 632 cussions on ice sheet datasets. The authors acknowledge reviewers for their kind comments which have helped to improve
 633 the manuscript presentation.

634 **References**

- 635 1. S. Arlot, A. Celisse, et al. A survey of cross-validation procedures for model selection. *Statistics surveys*, 4:40–79, 2010.
- 636 2. D. B. Bahr, W. T. Pfeffer, and G. Kaser. Glacier volume estimation as an ill-posed inversion. *Journal of Glaciology*, 60(223):922–934, 2014.
- 637 3. J. Bamber, J. Griggs, R. Hurkmans, J. Dowdeswell, S. Gogineni, I. Howat, J. Mouginot, J. Paden, S. Palmer, E. Rignot, et al. A new bed elevation
 638 dataset for greenland. *The Cryosphere*, 7(2):499–510, 2013.
- 639 4. JL Bamber, JL Gomez-Dans, and JA Griggs. A new 1 km digital elevation model of the antarctic derived from combined satellite radar and laser
 640 data—part 1: Data and methods. *The Cryosphere*, 3(1):101–111, 2009.
- 641 5. Andrew F Bennett. *Inverse modeling of the ocean and atmosphere*. Cambridge University Press, 2005.
- 642 6. M. Boutounet, J. Monnier, and J.-P. Vila. Multi-regime shallow free surface laminar flow models for quasi-newtonian fluids. *European Journal of*
 643 *Mechanics-B/Fluids*, 55:182–206, 2016.
- 644 7. D. Brinkerhoff, A. Aschwanden, and M. Truffer. Bayesian inference of subglacial topography using mass conservation. *Frontiers in Earth Science*,
 645 4:8, 2016.
- 646 8. W.F. Budd and I.F. Allison. An empirical scheme for estimating the dynamics of unmeasured glaciers. In *Proceedings of the Moscow Symposium*
 647 *Snow and Ice*, pages 246–256, 1975.
- 648 9. G. Clarke, E. Berthier, C. Schoof, and A. Jarosch. Neural networks applied to estimating subglacial topography and glacier volume. *Journal of*
 649 *Climate*, 22(8):2146–2160, 2009.
- 650 10. L. Dalc n, R. Paz, and M. Storti. Mpi for python. *Journal of Parallel and Distributed Computing*, 65(9):1108–1115, 2005.
- 651 11. V Demyanov, M Kanevsky, S Chernov, E Savelieva, and V Timonin. Neural network residual kriging application for climatic data. *Journal of*
 652 *Geographic Information and Decision Analysis*, 2(2):215–232, 1998.
- 653 12. D. Farinotti, D. Brinkerhoff, D. Clarke, J. F rst, H. Frey, P. Gantayat, F. Gillet-Chaulet, C. Girard, M. Huss, P. Leclercq, et al. How accurate are
 654 estimates of glacier ice thickness ? results from itmix, the ice thickness models intercomparison experiment. *The Cryosphere*, 11(2):949–970,
 655 2017.
- 656 13. Christopher J Fogwill, Christian SM Turney, Katrin J Meissner, Nicholas R Golledge, Paul Spence, Jason L Roberts, Mathew H England, Richard T
 657 Jones, and Lionel Carter. Testing the sensitivity of the east antarctic ice sheet to southern ocean dynamics: past changes and future implications.
 658 *Journal of Quaternary Science*, 29(1):91–98, 2014.
- 659 14. P. Fretwell, H. Pritchard, D. Vaughan, J. Bamber, N. Barrand, R. Bell, C. Bianchi, R. Bingham, D. Blankenship, G. Casassa, et al. Bedmap2:
 660 improved ice bed, surface and thickness datasets for antarctica. *The Cryosphere*, 7(1), 2013.
- 661 15. C. Geuzaine and J.-F. Remacle. Gmsh: A 3-d finite element mesh generator with built-in pre-and post-processing facilities. *International journal*
 662 *for numerical methods in engineering*, 79(11):1309–1331, 2009.
- 663 16. X. Glorot, A. Bordes, and Y. Bengio. Deep sparse rectifier neural networks. In *Proceedings of the fourteenth international conference on artificial*
 664 *intelligence and statistics*, pages 315–323, 2011.

- 665 17. R. Greve and H. Blater. *Dynamics of Ice Sheets and Glaciers*. Advances in Geophysical and Environmental Mechanics and Mathematics. Springer-
666 Verlag, 2009.
- 667 18. G. Gudmundsson. Transmission of basal variability to a glacier surface. *Journal of Geophysical Research: Solid Earth*, 108(B5), 2003.
- 668 19. G. Gudmundsson. Analytical solutions for the surface response to small amplitude perturbations in boundary data in the shallow-ice-stream
669 approximation. *The Cryosphere*, 2(2):77–93, 2008.
- 670 20. S.A. Haben, A.S. Lawless, and N.K. Nichols. Conditioning of incremental variational data assimilation, with application to the met office system.
671 *Tellus A: Dynamic Meteorology and Oceanography*, 63(4):782–792, 2011.
- 672 21. C. Heining and M. Sellier. Direct reconstruction of three-dimensional glacier bedrock and surface elevation from free surface velocity. *AIMS*
673 *Geosciences*, 2:45–63, 2016.
- 674 22. V. Helm, A. Humbert, and H. Miller. Elevation and elevation change of greenland and antarctica derived from cryosat-2. *The Cryosphere*,
675 8(4):1539–1559, 2014.
- 676 23. R. Hindmarsh. A numerical comparison of approximations to the stokes equations in ice sheet and glacier modeling. *J. geophysical research*, 109,
677 2004.
- 678 24. R. Hindmarsh. Stress gradient damping of thermoviscous ice flow instabilities. *Journal of Geophysical Research: Solid Earth*, 111(B12), 2006.
- 679 25. M. Huss and D. Farinotti. A high-resolution bedrock map for the antarctic peninsula. *The Cryosphere*, 8(4):1261–1273, 2014.
- 680 26. M.F. Hutchinson. A new procedure for gridding elevation and stream line data with automatic removal of spurious pits. *Journal of hydrology*,
681 106(3-4):211–232, 1989.
- 682 27. D. Jansen, H. Sandhäger, and W. Rack. Model experiments on large tabular iceberg evolution: ablation and strain thinning. *Journal of glaciology*,
683 51(174):363–372, 2005.
- 684 28. B. Kaltenbacher, A. Neubauer, and O. Scherzer. *Iterative regularization methods for nonlinear ill-posed problems*, volume 6. Walter de Gruyter,
685 2008.
- 686 29. B. Kamb and K. Echelmeyer. Stress-gradient coupling in glacier flow: I. longitudinal averaging of the influence of ice thickness and surface slope.
687 *Journal of Glaciology*, 32(111):267–284, 1986.
- 688 30. M. Kanevski, V. Timonin, and A. Pozdnukhov. *Machine learning for spatial environmental data: theory, applications, and software*. EPFL press,
689 2009.
- 690 31. D. Kingma and J. Ba. Adam: A method for stochastic optimization. *arXiv preprint arXiv:1412.6980*, 2014.
- 691 32. Y. LeCun, Y. Bengio, and G. Hinton. Deep learning. *nature*, 521(7553):436, 2015.
- 692 33. A. Lorenc. Optimal nonlinear objective analysis. *Quarterly Journal of the Royal Meteorological Society*, 114(479):205–240, 1988.
- 693 34. N. Martin and J. Monnier. Adjoint accuracy for the full-stokes ice flow model: limits to the transmission of basal friction variability to the surface.
694 *The Cryosphere*, 8:721–741, 2014.
- 695 35. N. Martin and J. Monnier. Inverse rheometry and basal properties inference for pseudoplastic geophysical flows. *European Journal of Mechanics-*
696 *B/Fluids*, 50:110–126, 2015.
- 697 36. L. Michel, M. Picasso, D. Farinotti, A. Bauder, M. Funk, and H. Blatter. Estimating the ice thickness of mountain glaciers with an inverse approach
698 using surface topography and mass-balance. *Inverse Problems*, 29(3):035002, 2013.
- 699 37. L. Michel, M. Picasso, D. Farinotti, M. Funk, and H. Blatter. Estimating the ice thickness of shallow glaciers from surface topography and
700 mass-balance data with a shape optimization algorithm. *Computers & Geosciences*, 66:182–199, 2014.
- 701 38. J. Monnier and P.-E. des Bosc. Inference of the bottom properties in shallow ice approximation models. *Inverse Problems*, 33(11):115001, 2017.
- 702 39. J. Monnier and J. Zhu. Inference of the bottom topography in anisothermal mildly-sheared shallow ice flows. *Computer Methods in Applied*
703 *Mechanics and Engineering*, 348:954–977, 2019.
- 704 40. M. Morlighem, E. Rignot, J. Mouginot, H. Seroussi, and E. Larour. High-resolution ice-thickness mapping in south greenland. *Annals of Glaciol-*
705 *ogy*, 55(67):64–70, 2014.
- 706 41. M. Morlighem, E. Rignot, H. Seroussi, E. Larour, H. Ben Dhia, and D. Aubry. A mass conservation approach for mapping glacier ice thickness.
707 *Geophysical Research Letters*, 38(19), 2011.
- 708 42. M. Morlighem, C. Williams, E. Rignot, L. An, J.E. Arndt, J. Bamber, G. Catania, N. Chauché, J. Dowdeswell, B. Dorschel, et al. Bedmachine
709 v3: Complete bed topography and ocean bathymetry mapping of greenland from multibeam echo sounding combined with mass conservation.
710 *Geophysical research letters*, 44(21), 2017.
- 711 43. J. Mouginot, E. Rignot, B. Scheuchl, and R. Millan. Comprehensive annual ice sheet velocity mapping using landsat-8, sentinel-1, and radarsat-2
712 data. *Remote Sensing*, 9(4):364, 2017.
- 713 44. P.B. Price, O. Nagornov, R. Bay, D. Chirkin, Y. He, P. Miocinovic, A. Richards, K. Woschnagg, B. Koci, and V. Zagorodnov. Temperature profile
714 for glacial ice at the south pole: Implications for life in a nearby subglacial lake. *Proceedings of the National Academy of Sciences*, 99(12):7844–
715 7847, 2002.
- 716 45. U. Radok, D. Jenssen, and W. Budd. Steady-state temperature profiles in ice sheets. *Bull. Int. Assoc. Scient. Hydrol*, 8(1):36, 1970.
- 717 46. L. Rasmussen. Bed topography and mass-balance distribution of columbia glacier, alaska, usa, determined from sequential aerial photography.
718 *Journal of Glaciology*, 34(117):208–216, 1988.
- 719 47. C. Schoof and C. Hindmarsh. Thin-film flows with wall slip: an asymptotic analysis of higher order glacier flow models. *Q. J. Mech. Appl. Math.*,
720 63(1):73–114, 2010.
- 721 48. M. Sellier. Inverse problems in free surface flows: a review. *Acta Mechanica*, 227(3):913–935, 2016.
- 722 49. H. Seroussi, M. Morlighem, E. Rignot, A. Khazendar, E. Larour, and J. Mouginot. Dependence of century-scale projections of the greenland ice
723 sheet on its thermal regime. *Int. Glacio. Soc.*, 59:1024–1034, 2013.
- 724 50. N. Srivastava, G. Hinton, A. Krizhevsky, I. Sutskever, and R. Salakhutdinov. Dropout: a simple way to prevent neural networks from overfitting.
725 *The Journal of Machine Learning Research*, 15(1):1929–1958, 2014.
- 726 51. W. Van Pelt, J. Oerlemans, C. Reijmer, R. Pettersson, V. Pohjola, E. Isaksson, D. Divine, et al. An iterative inverse method to estimate basal
727 topography and initialize ice flow models. *The Cryosphere*, 7:987–1006, 2013.
- 728 52. J.M. van Wessem, W. Jan Van De Berg, B. Noël, E. Van Meijgaard, C. Amory, G. Birnbaum, C. Jakobs, K. Krüger, J. Lenaerts, S. Lhermitte, et al.
729 Modelling the climate and surface mass balance of polar ice sheets using racmo2: Part 2: Antarctica (1979-2016). *The Cryosphere*, 12(4):1479–
730 1498, 2018.
- 731 53. G. Wahba. *Spline models for observational data*, volume 59. SIAM, 1990.
- 732 54. R. Williams, R. Hindmarsh, and R. Arthern. Calculating balance velocities with a membrane stress correction. *Journal of Glaciology*, 60(220):294–
733 304, 2014.
- 734 55. R. Winkelmann, M.A. Martin, M. Haseloff, T. Albrecht, E. Bueler, C. Khroulev, and A. Levermann. The potsdam parallel ice sheet model
735 (pism-pik) part 1: Model description. *The Cryosphere*, 5(3):715–726, 2011.

Table 8 Domain Ω_p =Ant2, information and results.

Domain Ω_p & mesh information			
Surface $ \Omega_p $	431860 km ²		
Mean ice thickness of h_b (Bedmap2)	2144.4 m		
# mesh vertices: in Ω_p / on flight tracks	65123/5194		
RU-SIA model output (with $\hat{\gamma}$)			
	Median	Mean	Max
$ H(h_b) - H^{obs} $ (before h -inversion)	8.7 m	17.3 m	149.9 m
$ H(h^*) - H^{obs} $ (after h -inversion)	3.9 m	5.1 m	49.2 m
Inferred RHS \dot{a}			
$ \dot{a}^* - \dot{a}_b $	0.6 cm/y	0.8 cm/y	4.0 cm/y
$ \dot{a}^* - \dot{a}_b / \dot{a}_b $	14.8 %	13.2 %	20 %
Inferred thickness h			
$ h^* - h_b $	171.1 m	302.4 m	2025.6 m
$ h^* - h_b / h_b $	8.3 %	14.2 %	80.0 %
Ice volume change in km ³ / in %	5.2 10 ⁴ km ³ / 5.6 %		

Table 9 Domain Ω_p =Ant4, information and results.

Domain Ω_p & mesh information			
Surface $ \Omega_p $	439045 km ²		
Mean ice thickness of h_b (Bedmap2)	2745.4 m		
# mesh vertices: in Ω_p / on flight tracks	61219/4977		
RU-SIA model output (with $\hat{\gamma}$)			
	Median	Mean	Max
$ H(h_b) - H^{obs} $ (before h -inversion)	6.3 m	8.4 m	66.9 m
$ H(h^*) - H^{obs} $ (after h -inversion)	3.0 m	4.1 m	45.3 m
Inferred RHS \dot{a}			
$ \dot{a}^* - \dot{a}_b $	2.0 cm/y	2.7 cm/y	15.0 cm/y
$ \dot{a}^* - \dot{a}_b / \dot{a}_b $	8.7 %	10.1 %	20 %
Inferred thickness h			
$ h^* - h_b $	147.6 m	185.0 m	1241.6 m
$ h^* - h_b / h_b $	5.7 %	7.0 %	50.4 %
Ice volume change in km ³ / in %	1.5 10 ⁴ km ³ / 1.5 %		

736 A Results for other EAIS areas

737 In this section, the estimation of ice thickness is performed in the four other areas indicated in Fig. 4: Ant2, Ant4, Ant5 and Ant6. Ant2 is located
738 upstream of Fisher and Merllor ice-streams (upstream Amery ice shelf). Ant4 is located upstream Totten ice-streams (Wilkes land and Terre Ad lie),
739 one of the largest discharger of ice in EAIS. Ant5 is located upstream Ninnis and Mertz ice-streams in Terre Ad lie and George V land. Ant6 is located
740 upstream Byrd ice-streams (east of Ross Ice shelf), see Fig. 4.

741 These areas have been relatively well covered during the airborne campaigns excepted the north-east part of Ant2, see Fig. 12. Distances between flight
742 tracks are relatively low, therefore the empirical uncertainty assigned to Bedmap2 estimations h_b is low too: $\approx \pm[100 - 250]$ m, see figures 12, 13, 14,
743 15 (Middle).

744 For each area, domain information and statistics on the numerical results are presented, see tables 8-11.

745 As already noticed, RU-SIA model already fits well with the surface topography after the data-driven model (Step 2) only; that is with $\hat{\gamma}$ and h_b as
746 parameters in (1): see lines " $|H(h_b) - H_{obs}|$ (before h -inversion)" in the tables. Next RU-SIA model fits accurately the surface topography after the
747 re-calibration / estimation of h . Indeed, misfit values range within $\approx [4 - 5]$ m in mean; see lines " $|H(h_b) - H_{obs}|$ (after h -inversion)" in tables.

748 The corrections made on \dot{a} are $\sim [10 - 17]$ % in mean, that is within the a-priori uncertainty range indicated in [52].

749 The estimated thickness h^* is plotted in each case, see figures 12-15 (Down)(L); its difference with h_b is plotted (Down)(R). The corrections made
750 to h_b are non negligible: they are ranging within $[7.0 - 15.9]$ % in mean (corresponding to $[185 - 373]$ m, see the lines " $|h^* - h_b|$ " in tables). These
751 corrections lead to changes of total ice volume by $[1.5, 5.6]$ %. Again, the obtained difference with h_b is independent of the distance to the closest flight
752 track. Maximum values of correction to h_b can be locally high. In the uncovered north-east Ant2 area, corrections are up to ≈ 2000 m. At ≈ 50 km from
753 the nearest flight track (that is ~ 2 minimal wave lengths of the model) correction may reach 1000m (even in area surrounded by well covered areas),
754 see e.g. figures 14 and 15 (Down)(R). Beyond ≈ 100 km from the nearest data, the correction of h_b may be significant or not, depending on the surface
755 signature, see e.g. figures 14 and 15 (Down)(R).

756

Table 10 Ant 5, information and results.

Domain Ω_p & mesh information			
Surface $ \Omega_p $	362019 km^2		
Mean ice thickness of h_b (Bedmap2)	2415.3 m		
# mesh vertices: in Ω_p / on flight tracks	41597/2351		
RU-SIA model output (with $\hat{\gamma}$)	Median	Mean	Max
$ H(h_b) - H^{obs} $ (before h -inversion)	18.3 m	23.9 m	173.3 m
$ H(h^*) - H^{obs} $ (after h -inversion)	3.9 m	5.1 m	43.1 m
Inferred RHS \dot{a}			
$ \dot{a}^* - \dot{a}_b $	3.9 cm/y	4.4 cm/y	14.5 cm/y
$ \dot{a}^* - \dot{a}_b / \dot{a}_b $	18.8 %	15.4 %	20 %
Inferred thickness h			
$ h^* - h_b $	275.1 m	373.1 m	1989.2 m
$ h^* - h_b / h_b $	12.1 %	15.9 %	68.8 %
Ice volume change in km^3 / in %	3.8 $10^4 km^3$ / 5.6 %		

Table 11 Domain Ω_p =Ant6, information and results.

Domain Ω_p & mesh information			
Surface $ \Omega_p $	406388 km^2		
Mean ice thickness of h_b (Bedmap2)	2672.9 m		
# mesh vertices: in Ω_p / on flight tracks	63981/3012		
RU-SIA model output (with $\hat{\gamma}$)	Median	Mean	Max
$ H(h_b) - H^{obs} $ (before h -inversion)	8.3 m	11.0 m	46.8 m
$ H(h^*) - H^{obs} $ (after h -inversion)	2.7 m	3.4 m	21.3 m
Inferred RHS \dot{a}			
$ \dot{a}^* - \dot{a}_b $	0.4 cm/y	0.5 cm/y	1.8 cm/y
$ \dot{a}^* - \dot{a}_b / \dot{a}_b $	15.8 %	14.2 %	20 %
Inferred thickness h			
$ h^* - h_b $	218.6 m	313.9 m	1777.3 m
$ h^* - h_b / h_b $	8.1 %	11.6 %	63.8 %
Ice volume change in km^3 / in %	2.6 $10^3 km^3$ / 1.7 %		

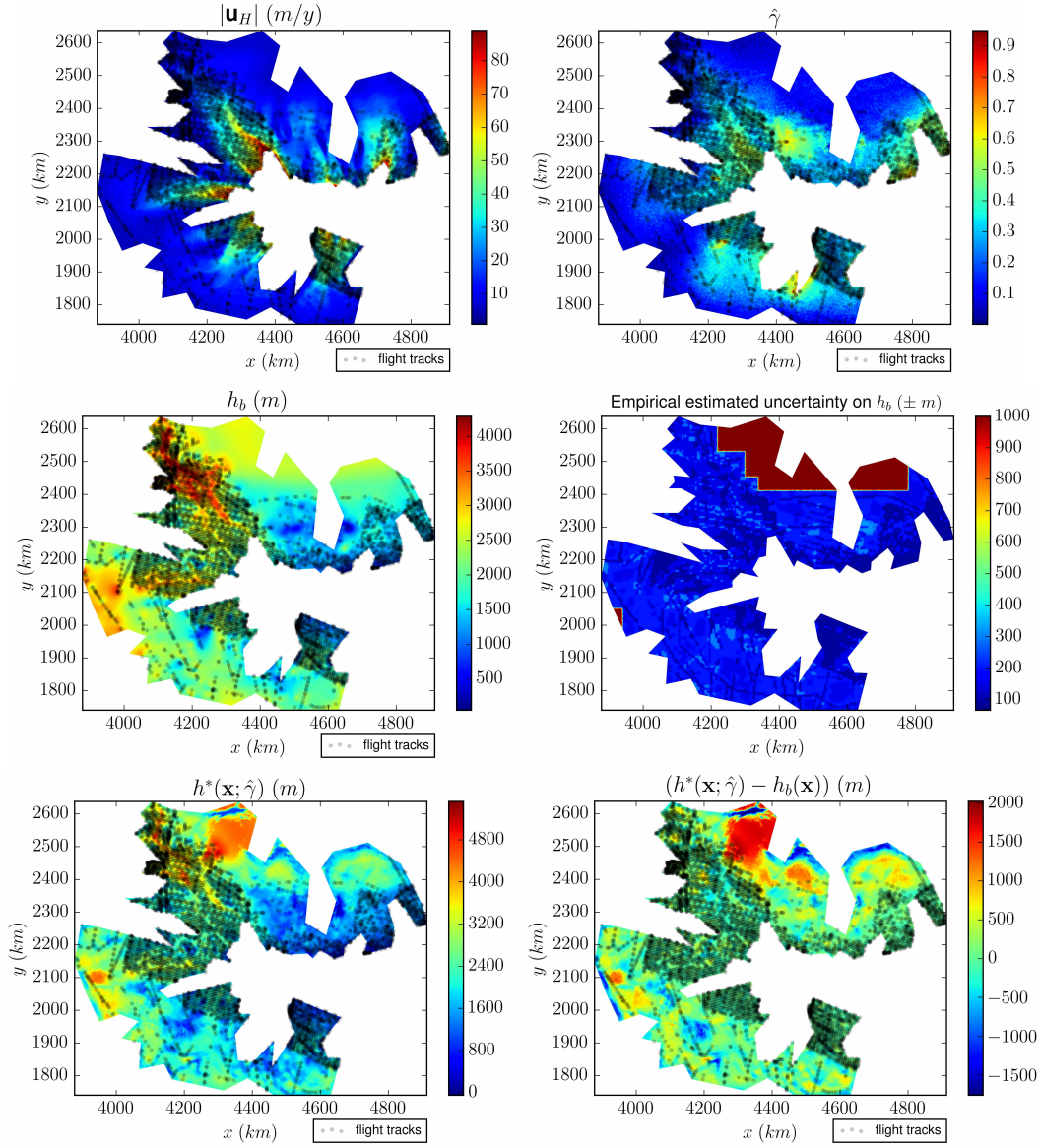


Fig. 12 Domain $\Omega_p=Ant2$ (the plotted coordinates equal the Eastings-Northings plus (2800,2800)km): (Up)(L) Surface velocity module $|\mathbf{u}_H|$ and flight tracks. (R) $\hat{\gamma}$ computed by NNRK, see (11). (Middle)(L) Thickness h_b from Bedmap2 [14]. (R) Empirical uncertainty on h_b from [14]. (Down)(L) Inferred thickness with $\hat{\gamma}$: $h^*(\hat{\gamma})$. (R) Difference $(h^*(\hat{\gamma}) - h_b)$.

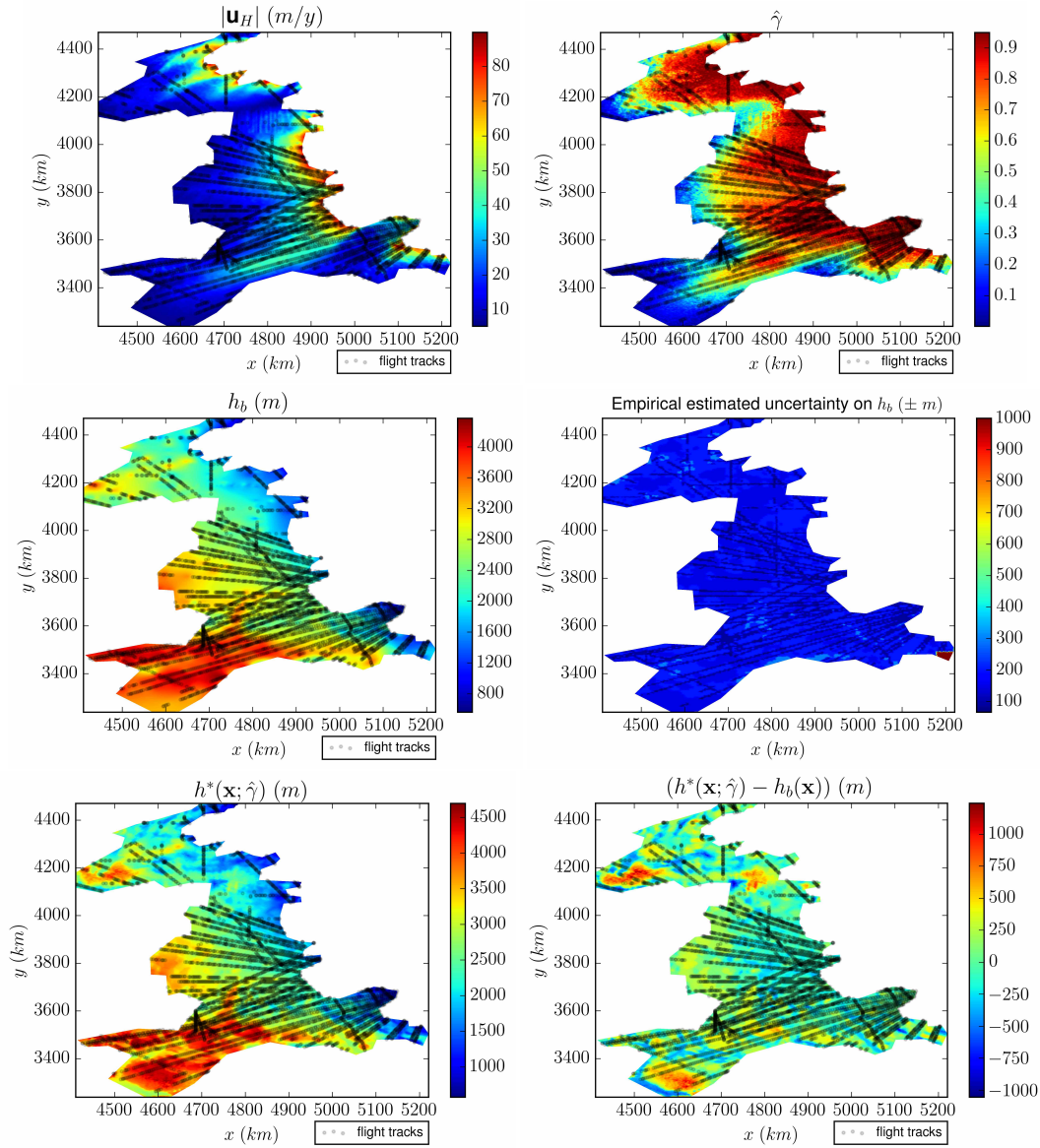


Fig. 13 Domain $\Omega_p=Ant4$ (the plotted coordinates equal the Eastings-Northings plus (2800,2800)km): (Up)(L) Surface velocity module $|\mathbf{u}_H|$ and flight tracks. (R) $\hat{\gamma}$ computed by NNRK, see (11). (Middle)(L) Thickness h_b from Bedmap2 [14]. (R) Empirical uncertainty on h_b from [14]. (Down)(L) Inferred thickness with $\hat{\gamma}$: $h^*(\hat{\gamma})$. (R) Difference $(h^*(\hat{\gamma}) - h_b)$.

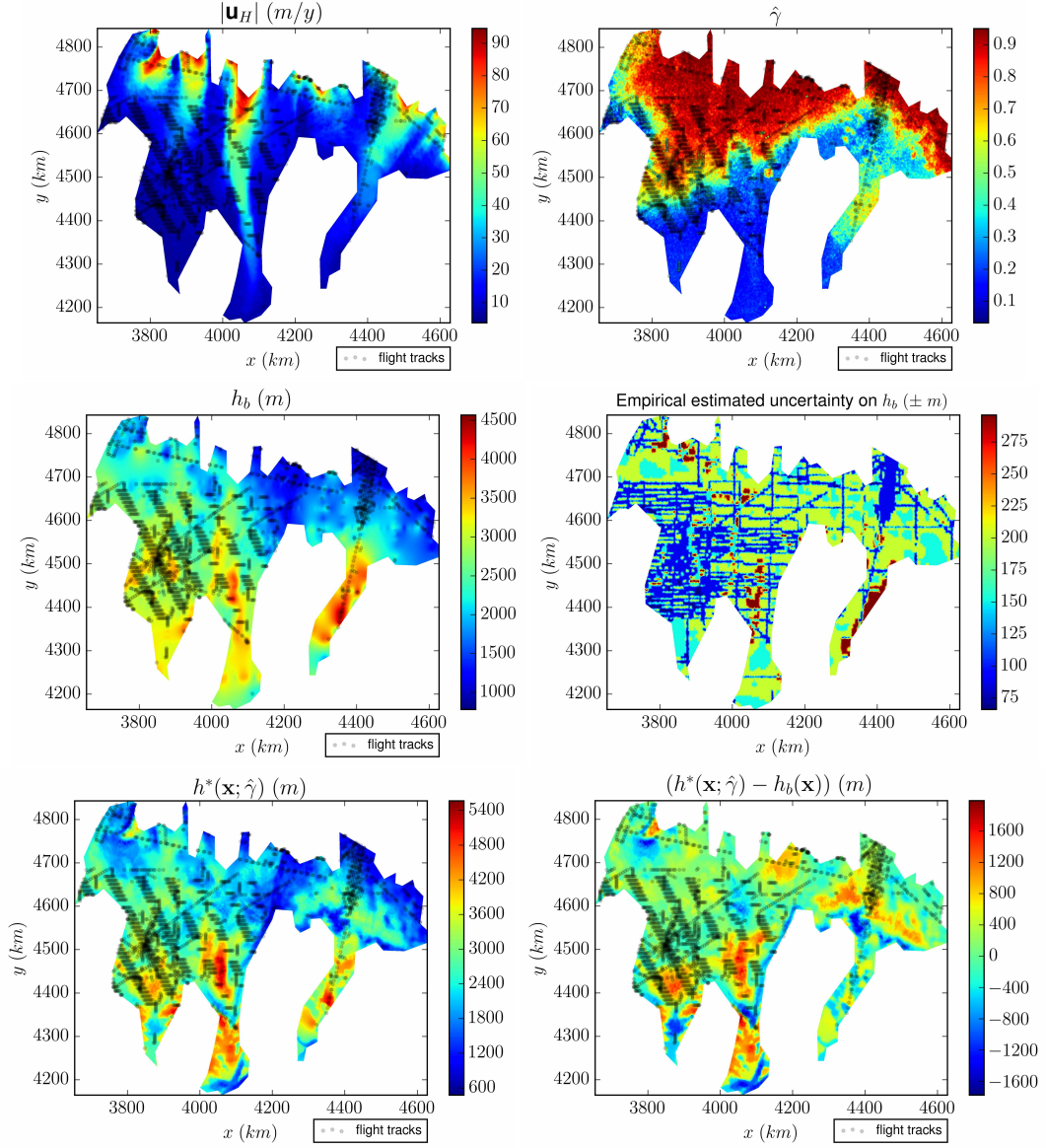


Fig. 14 Domain $\Omega_p=\text{Ant5}$ (the plotted coordinates equal the Eastings-Northings plus (2800,2800)km): (Up)(L) Surface velocity module $|\mathbf{u}_H|$ and flight tracks. (R) $\hat{\gamma}$ computed by NNRK, see (11). (Middle)(L) Thickness h_b from Bedmap2 [14]. (R) Empirical uncertainty on h_b from [14]. (Down)(L) Inferred thickness with $\hat{\gamma}$: $h^*(\hat{\gamma})$. (R) Difference $(h^*(\hat{\gamma}) - h_b)$.

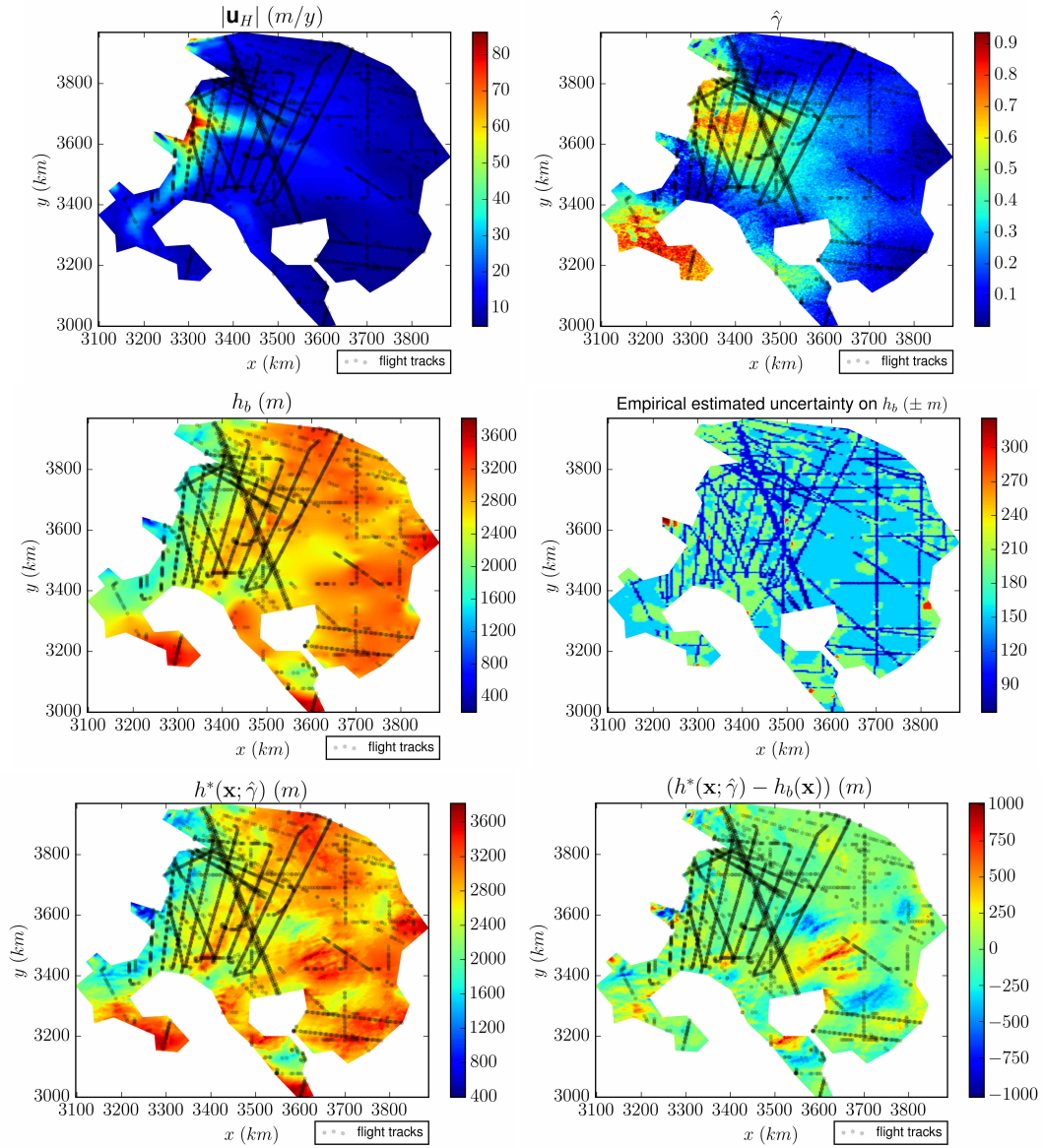


Fig. 15 Domain $\Omega_p = \text{Ant6}$ (the plotted coordinates equal the Eastings-Northings plus (2800, 2800)km): (Up)(L) Surface velocity module $|\mathbf{u}_H|$ and flight tracks. (R) $\hat{\gamma}$ computed by NNRK, see (11). (Middle)(L) Thickness h_b from Bedmap2 [14]. (R) Empirical uncertainty on h_b from [14]. (Down)(L) Inferred thickness with $\hat{\gamma}$: $h^*(\hat{\gamma})$. (R) Difference $(h^*(\hat{\gamma}) - h_b)$.